Astron. Astrophys. 338, 881–896 (1998)

ASTRONOMY AND ASTROPHYSICS

# B stars and the chemical evolution of the Galactic disk⋆

**C.A. Gummersbach, A. Kaufer, D.R. Schäfer, T. Szeifert, and B. Wolf**

Landessternwarte Heidelberg-Königstuhl, Königstuhl 12, D-69117 Heidelberg, Germany (C.Gummersbach@lsw.uni-heidelberg.de)

Received 15 May 1998 / Accepted 12 August 1998

**Abstract.** We determine stellar parameters and He, C, N, O, Mg, Al, and Si abundances of a sample of 16 early B main-sequence stars in galactocentric distances of $R_{\rm GC} = 5$–$14$ kpc by reanalyzing and extending the observations of Kaufer et al. (1994) towards the Galactic center. The analysis uses Kurucz ATLAS 9 LTE atmospheres and Giddings-Butler DETAIL/SURFACE non-LTE line formation.

It is shown that beside non-LTE effects the metallicity of the underlying atmosphere has a non-negligible impact on the temperature structure and the subsequent line formation. The local field is found to have an underabundance of about $-0.2$dex relative to the Sun. Contrary to part of recent B-star and H II-region determinations we derive an oxygen abundance gradient $\Delta[\mathrm{O/H}]/\Delta R_{\rm GC} = (-0.07 \pm 0.02)\ \mathrm{dex/kpc}$ for the Galactic disk, typical for normal spiral galaxies of similar Hubble type.

This steep gradient is in contrast to the recent evidence that *(a)* our Milky Way is actually a barred spiral galaxy, and *(b)* barred galaxies generally have almost flat abundance gradients throughout their disks. Comparing our results with numerical models of the chemodynamical evolution of barred galaxies we derive an age of about 1 Gyr for the central bar structure of the Galaxy. We argue that our bar is still too young to exert a notable flattening effect on the chemical abundance gradient of the Galactic disk.

**Key words:** stars: abundances – stars: early-type – stars: fundamental parameters – Galaxy: abundances – Galaxy: evolution

## 1. Introduction

The chemodynamical evolution of the Galaxy is a key element of cosmic chemical evolution. Theoretical models of Galactic evolution (e.g. Tosi 1996; Matteucci 1996) are aimed to predict quantities as the age-metallicity relation in the solar neighborhood and the abundance gradients along the Galactic disk. However, these models are still hampered by a series of relatively free input parameters—initial-mass function, star-formation rate, stellar yields, infall or galactic winds, and radial inflows or outflows. A complementary way to reconstruct the chemical history of the Milky Way is to look for the abundance pattern of stellar populations of different ages and positions inside the Galaxy (see Pagel 1997 and McWilliam 1997 for general reviews). These can be compared with the metallicities of external spiral galaxies of similar morphological type.

The present paper is organized as follows. Sects. 2 and 3 comprise an extended introduction given the many ramifications of the subject. In Sect. 2 the observational evidence for abundance gradients in both normal and barred spirals is reviewed and confronted with results from stellar populations of different age in the Galactic disk. In Sect. 3 the various models of B-star analyses are discussed. The adopted atmosphere and line-formation models are described in Sects. 4, 5, and 6. Sect. 7 presents the applied method of analysis. Sect. 8 introduces the sample of observed B stars and provides the derived stellar parameters and chemical abundances. A final discussion is given in Sect. 9.

## 2. Abundance patterns in spiral galaxies

### *2.1. Abundance gradients in normal spiral galaxies*

Contrary to elliptical galaxies, where due to the absence of young stellar objects one has to rely on integrated colors and spectra of the entire stellar population, in spiral galaxies one can use the observations of single H II regions to derive metal abundances. For a good spatial resolution face-on galaxies like M 33, M 81, or M 101 are preferred targets. In these normal spirals without a bar structure the following global abundance patterns are derived. The abundance gradient in early-type spirals (Sa/Sb) is about $-0.05\ \mathrm{dex/kpc}$, in late-type spirals (Sc) about $-0.15\ \mathrm{dex/kpc}$. The Galactic type Sbc has a typical gradient of about $-0.07\,\mathrm{dex/kpc}$ (Belley & Roy 1992; Vila-Costas & Edmunds 1992; Oey & Kennicutt 1993; Zaritsky et al. 1994).

The slope of the logarithmic gradient is generally constant along the galactic disk corresponding to an exponential decrease of the abundance (Henry & Howard 1995). The characteristic abundance, e.g. extrapolated up to the center of the galaxy, decreases versus later Hubble types. Skillman et al. (1996) emphasize the influence of the surrounding galaxy-cluster medium.

*Send offprint requests to*: C.Gummersbach@lsw.uni-heidelberg.de

⋆ Based on observations collected at the European Southern Observatory, La Silla, Chile, and at the German-Spanish Astronomical Center, Calar Alto, Spain.

**Table 1.** Observed abundance gradients in the Galactic disk

| Objects | Age [Gyr] | Gal. Distance [kpc] | Metallicity Gradients [dex/kpc] | References |
|---|---|---|---|---|
| Old open clusters | 1–10 | 6.5–16 | $-0.07 \ldots -0.10$ | Friel (1995), Twarog et al. (1997) |
| FG main-sequence stars | 2–10 | 6–11 | $-0.07$ | Edvardsson et al. (1993) |
| Planetary nebulae | 4–6 | 5–12 | $-0.06$ | Maciel & Köppen (1994) |
| H II regions | 0.001–0.01 | 7–14 | $-0.07 \ldots -0.09$ | Shaver et al. (1983) |
| | | 0–11 | $-0.06 \ldots -0.07$ | Afflerbach et al. (1996, 1997) |
| | | 0–16 | $-0.11$ | Rudolph et al. (1997) |
| | | 11–18 | $\sim 0$ | Fich & Silkey (1991), Vílchez & Esteban (1996) |
| | | 6–10 | $\sim 0$ | Simpson et al. (1995) |
| B main-sequence stars | 0.001–0.01 | 6–18 | $-0.07$ | Smartt & Rolleston (1997) |
| | | 6–15 | $0 \ldots -0.03$ | Kaufer et al. (1994), Kilian-Montenbruck et al. (1994) |
| | | 5–14 | $-0.07$ | present study |

Galaxies at the center of clusters, which have lost most of its interstellar H I gas by interactions with neighboring galaxies and are shielded from infall of protogalactic matter, show flatter gradients and increased chemical abundances. First results of stellar spectroscopy in external spiral galaxies (Monteverde et al. 1997) agree with the H II-region results but still suffers larger errors.

### *2.2. Abundance gradients in barred spiral galaxies*

Two thirds of all spirals including our Galaxy possess a central bar structure (Sellwood & Wilkinson 1993). In recent years the chemical effects of such a bar have been systematically investigated. Vila-Costas & Edmunds (1992), Zaritsky et al. (1994), Martin & Roy (1994, 1995) and Roy et al. (1996) point out that the disks of barred spiral galaxies generally show flatter abundance gradients than normal spiral galaxies. Independently of Hubble type, vanishing gradients between $0$ and $-0.05 \mathrm{dex/kpc}$ are found. The absolute abundances, however, show the same correlation with Hubble type as non-barred galaxies.

In addition, Martin & Roy (1994) derive the following important relation: the stronger and the more elliptic the central bar structure the flatter the chemical gradient in the galactic disk. This result suggests that a pronounced bar leads to a homogenization of chemical composition in the entire galaxy. Numerical 3-D simulations of this chemodynamical evolution (Friedli et al. 1994; Friedli & Benz 1995; Martinet & Friedli 1997) indicate that matter inside the corotation radius flows towards the galactic center, and matter outside corotation flows outwards. The metal-poor inflow induces an enhanced star formation within the bar, which can lead to the formation of H II regions along the bar and to a nuclear starburst in the galactic center. The abundance gradient remains about constant or even increases in the innermost kpc. Contrary, the metal-rich outflow induces no enhanced star formation but a mere mixing, which flattens the abundance gradient in the galactic disk, even far outside the bar structure.

An indication for a young bar, therefore, is a break of the gradient (steep $\rightarrow$ flat) near the corotation radius of that galaxy. This behavior is now actually found in several barred galaxies (Martin & Roy 1995; Roy & Walsh 1997). An eventual second break (flat $\rightarrow$ steep) in the outskirts of the galaxy corresponding to the front of the outflow, however, has not been seen until now. The time scale of such a chemical mixing is relatively short in galactic standards, about 1 Gyr. Given a strong bar (ellipticity $b/a < 1/2$) a chemical disk gradient is able to flatten from $-0.10$ to $-0.02 \,\mathrm{dex/kpc}$ in only 500 Myr (Martinet & Friedli 1997).

The formation of the bar structure itself is ascribed to tidal interactions for early-type spirals and to disk instabilities for late-type spirals (Noguchi 1996). The corresponding time scale is also about 1 Gyr. Possibly, bar structures are temporary states during a secular evolution of normal spiral galaxies from late to early types, i.e., to bulge-dominated structures (Martinet 1995). This scenario would lead to a natural explanation for the flattening of the abundance gradients of unbarred spirals from late to early types: one or more bar phases in their history could have caused the chemical mixing in their disks.

### *2.3. Abundance gradients in the Galactic disk*

There has been growing evidence in recent years that also our Milky Way possesses a central bar structure (Kuijken 1996; Gerhard 1996; Gerhard et al. 1998; Raboud et al. 1998). Particularly, the near-infrared observations of the Diffuse Infrared Background Experiment (DIRBE) on board the COBE satellite show that the Galactic bulge is triaxial in shape. Its axis ratio is about $b/a = 1/2$ (Fux 1997; Gerhard et al. 1998). Furthermore, Raboud et al. (1998) find evidence for a general center-anticenter motion of stars in the solar neigbourhood of about $20 \,\mathrm{km\,s^{-1}}$ corresponding to the outflow expected for barred galaxies (Sect. 2.2). In this framework, inserting an ellipticity $E_{\mathrm{B}} = 10\,(1 - b/a) = 5$ in the above mentioned ellipticity-gradient correlation for barred galaxies (Martin & Roy 1994) yields a typical abundance gradient of the Galactic disk of $-0.03 \,\mathrm{dex/kpc}$.

Observationally, there are many determinations of the disk gradient from different stellar populations (Table 1). Old open

clusters with an age of $\tau = 1 - 10$ Gyr show a Fe gradient of $-0.07$ to $-0.10$) dex/kpc between $R_{\rm GC} = 6.5 - 16$ kpc (Carraro & Chiosi 1994; Friel 1995; Twarog et al. 1997). F and G main-sequence stars of $\tau = 2 - 10$ Gyr in the solar vicinity are observed by Edvardsson et al. (1993). Stellar orbits are statistically traced back using distance, proper motion, and a kinematic model of the Milky Way. The result is a constant Fe gradient of about $-0.07$ dex/kpc between $R_{\rm GC} = 6 - 11$kpc during the past Gyrs (Prantzos & Aubert 1995). Planetary nebulae of $\tau = 4-6$Gyr show an O gradient of $-0.06$dex/kpc between $R_{\rm GC} = 5 - 12$ kpc (Maciel & Köppen 1994).

In Galactic H II regions with $\tau = 10^6 - 10^7$ yr, however, the results are discordant. In their classical work Shaver et al. (1983) derive O and N gradients of $-0.07$ to $-0.09$ dex/kpc between $R_{\rm GC} = 7 - 14$ kpc. Afflerbach et al. (1996, 1997) find a gradient of $-0.06$ to $-0.07$ dex/kpc between $R_{\rm GC} = 0-11$kpc, Rudolph et al. (1997) a N gradient of $-0.11$dex/kpc between $R_{\rm GC} = 0-16$kpc. Contrary, Fich & Silkey (1991) and Vílchez & Esteban (1996) find a constant O and N abundance between $R_{\rm GC} = 11-18$kpc. Simpson et al. (1995) derive a flat gradient between $R_{\rm GC} = 6 - 10$ kpc. The situation is similar with the abundances of B main-sequence stars of $\tau = 10^6 - 10^7$ yr, as well. Smartt & Rolleston (1997) find an O gradient of $-0.07$dex/kpc between $R_{\rm GC} = 6-18$kpc, whereas Kaufer et al. (1994) and Kilian-Montenbruck et al. (1994) derive flat O and N gradients of 0 to $-0.03$dex/kpc between $R_{\rm GC} = 6-15$kpc.

### *2.4. A discrepancy: Is the Galactic abundance gradient $-0.02$ or $-0.07$ dex/kpc?*

At this point we are faced with a discrepancy. Observations of old stellar populations like old clusters, late-type stars, and Planetary nebulae, and part of the young H II regions and B stars indicate a rather steep Galactic abundance gradient of the order of $-0.07$ dex/kpc. This result would fit to a Milky Way seen as an ordinary, unbarred spiral galaxy of Hubble type Sbc. On the other side, part of the observations of young H II regions and B stars indicate a rather flat Galactic abundance gradient of the order of $-0.02$ dex/kpc. This result would fit to a Milky Way seen as a barred spiral galaxy of Hubble type SBbc and a bar axis ratio of about $b/a = 1/2$.

This apparent discrepancy could be explained, however, if the age of the Galactic bar structure is about the age of the young stellar populations. Then, the gradient-flattening effect of the bar could affect the youngest stellar generations only. To test this hypothesis it is crucial to determine the slope of the abundance gradient of the young stars in the Galactic disk, H II regions and B stars, whether it is really flat or not. In order to accomplish this task we decided to reanalyze the Kaufer et al. (1994) sample of early B main-sequence stars with non-LTE methods and to extend the sample by new observations between $R_{\rm GC} = 5 - 7$ kpc (Sect. 8).

## 3. Analysis of B stars

Generally, B stars are quite favorable objects for chemical-abundance analysis. Their photospheric spectra show lines of almost all important elements: H I, He I, C II, N II, O II, Mg II, Al III, Si II/III/IV, and Fe III. Contrary to late-type stars the spectral lines are relatively few in number and therefore mostly well separated. Due to the many line-free regions the continua are easily normalized, which is indispensable for reliable equivalent-width measurements. Furthermore, B stars on the main sequence show pure absorption spectra which are unaffected by stellar winds and intrinsic variability as seen in B supergiants (Kaufer 1998), Be stars (Rivinius et al. 1998), or B[e] stars (Gummersbach et al. 1995). As unevolved massive stars of about 10 $M_\odot$ early B main-sequence stars have an age of only about $10^7$ yr. So they reflect quite well the present state of chemical composition in the Galactic disk.

The aim of the spectroscopic analysis is a consistent determination of effective temperature $T_{\rm eff}$, gravity $\log g$, microturbulence $\xi$, projected rotational velocity $v \sin i$, and the chemical abundances $X_i$[1]. These stellar parameters enter a model by which the structure of the stellar atmosphere and the formation of spectral lines is computed and compared with the observed spectrum. A key point is the choice of this physical model. It is not yet clear if LTE (local thermodynamic equilibrium) can be assumed throughout the atmosphere or if departures from this approximation (non-LTE) have to be explicitly considered (e.g. Kudritzki & Hummer 1990). Another point are the line opacities (bound-bound absorptions) in use. Blanketing by spectral lines leads to a change of the radial temperature structure of the stars, i.e., backwarming and envelope cooling.

Which one of these two effects is more important for B stars is a matter of debate. The LTE atmosphere models of Kurucz (1979, 1993a) neglect a non-LTE treatment and promote a complete line blanketing with millions of considered lines. Contrary to the early non-LTE atmosphere models by Auer and Mihalas in the seventies it is now becoming possible to take line opacities into account in non-LTE models to some extent. However, analyses of Anderson (1985), Grigsby et al. (1992), Hubeny & Lanz (1992), and Dreizler & Werner (1993) show that this is computationally very costly and that the non-LTE radiation field with line blanketing are currently more similar to the LTE radiation field with line blanketing than to the non-LTE radiation field without line blanketing. In this way, we feel that it is a good compromise at the time being to use LTE atmospheres with complete line blanketing and a subsequent non-LTE line formation.

For B-star analyses various approaches are found in the literature. See Gehren (1988) for a general review of the subject. Kaufer et al. (1994) use ATLAS 8 LTE atmospheres (Kurucz 1979) and BHT (Baschek-Holweger-Traving) LTE line formation (Baschek et al. 1966). Kilian-Montenbruck et al. (1994) use the unpublished LTE atmospheres of Gold (1984) which

[1] Throughout this paper the chemical abundance of an element $i$ is denoted by $X_i \equiv 12 + \log(N_i/N_{\rm H})$, where $N_{\rm H}$ is the number density of hydrogen.

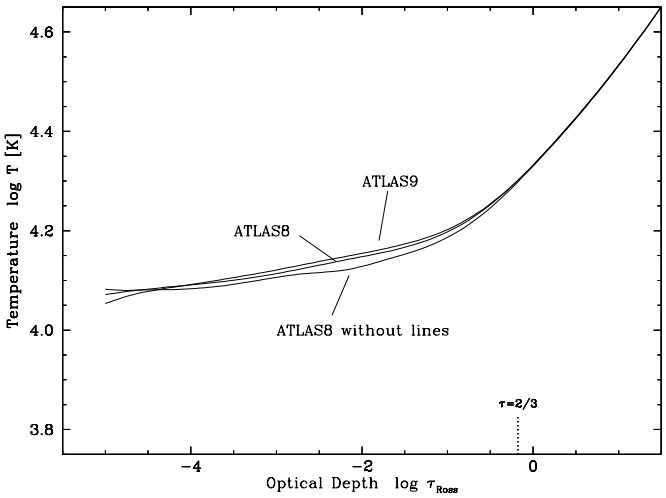


**Fig. 1.** ATLAS-version dependence of the temperature structure of a Kurucz model atmosphere. The ATLAS 9 model ($58{\cdot}10^9$ lines) is almost indistinguishable from the ATLAS 8 model ($1.7 \cdot 10^9$ lines). Both are well above the ATLAS 8 model without lines. The input parameters are $T_{\rm eff} = 20\,000$K, $\log g = 4.0, \xi = 2\mathrm{km\,s^{-1}}$, solar metallicity, LITTLE frequency grid, and 15 iterations, corresponding to a B main-sequence star.

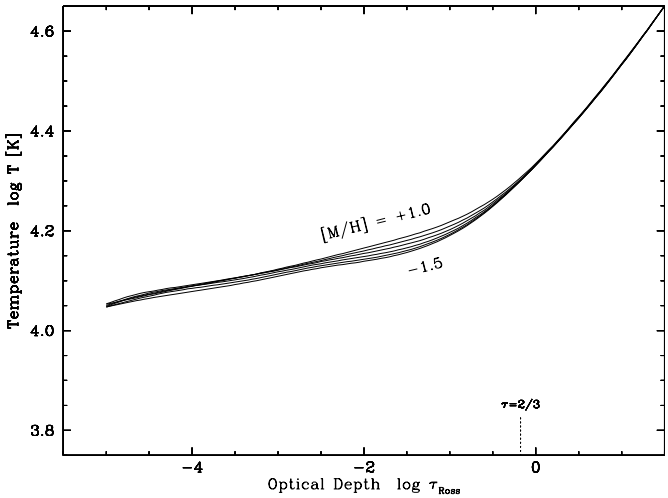


**Fig. 2.** Metallicity dependence of the temperature structure of a Kurucz model atmosphere. The effect of increasing metal abundance is clearly visible, especially in the line-formation region, $\log\tau = -2...0$. The input parameters are the same as in Fig. 1, computed with the ATLAS 9 code.

contain line opacities of only about 100 UV lines, and DETAIL/SURFACE non-LTE line formation (Giddings 1981; Butler & Giddings 1985). Smartt & Rolleston (1997) use ATLAS LTE atmospheres, as well. However, they use LTE line formation for the determination of $T_{\rm eff}$ and $\log g$ and, indirectly via the non-LTE O equivalent widths of Becker & Butler (1988b), DETAIL/SURFACE non-LTE line formation for the determination of the oxygen abundance.

In the present paper, we adopt the fully line-blanketed ATLAS 9 LTE atmospheres of Kurucz (1993a) in combination with DETAIL/SURFACE non-LTE line formation, reanalyzing and extending the Kaufer et al. (1994) sample. In this way, we want to clarify the possible improvements of both the update from ATLAS 8 to ATLAS 9 atmosphere models (Sect. 4) and from LTE to non-LTE line formation (Sect. 5). Furthermore, we will check the silent assumption made in all recent B-star studies that the metallicity of the underlying atmosphere has no impact on line formation. Otherwise, the abundance derived from spectral-line analysis should well agree with the abundance used in the atmosphere calculation.

Just to mention, there are a growing number of interesting alternative approaches for spectral-line analyses, e.g. pure pattern-recognition methods as the neural-network approach of Bailer-Jones et al. (1997), which yields temperatures and rough metallities.

## 4. ATLAS 9 LTE atmospheres

### *4.1. Implementation*

The broadly used Kurucz ATLAS codes produce models of plane-parallel stellar atmospheres in local thermodynamic equilibrium. A key input are the opacity distribution functions (ODFs) describing the bound-bound transitions which are necessary to account for an accurate treatment of line blanketing. In his ATLAS 6 and ATLAS 8 models Kurucz (1979) used 1.7 million spectral lines. The recent ATLAS 9 models of Kurucz (1991ab, 1992, 1993a), however, contain ODFs computed from 58 millions lines.

For platform reasons, instead of using the original VMS/VAX ATLAS 9 version of Kurucz (1993a) we adopted the UNIX version of Lemke (1995) which can be found on the anonymous FTP server of the Collaborative Computational Project No. 7 (CCP7)—The Analysis of Astronomical Spectra (Jeffery 1996). In this setup effective temperature, gravity, microturbulence, metallicity, type of frequency grid, number of iterations, number of depth levels, depth range, and mixing-length parameter can all be directly entered in command-line mode. The ATLAS 9 ODFs of different metallicities and microturbulences are read from the relevant CD-ROMs (Kurucz 1993bc) during the calculation. To cover a broad range in optical depth we used all 64 possible depth levels and a depth interval from $\log\tau = -5...+4$.

### *4.2. Parameter study*

At this point, it is very instructive to perform a systematic study of the influence of the relevant parameters entering the program. This includes the update from ATLAS 8 to ATLAS 9, the stellar input parameters $T_{\rm eff}$, $\log g$, $\xi$, and metallicity, as well as computational parameters like the number of numerical iterations or the choice of the frequency grid in use. In this way, it is possible for the problem given, to discern parameters relevant for the atmosphere structure from negligible ones. Apart from the basic dependencies on $T_{\rm eff}$ and $\log g$ the effect of the other parameters is not so obvious. In the following we quote the most important results.

(*a)* The *version of the* ATLAS *code* is of minor importance. Fig. 1 shows the run of temperature $T$ as function of Rosseland optical depth $\tau_{\rm Ross}$ in the atmosphere. The input parameters are typical values for an early B main-sequence star. The effect of line blanketing—backwarming in deeper layers and envelope cooling in the outer layers—is evident. However, the difference between the ATLAS 8 and ATLAS 9 models is small compared to the difference to the ATLAS model without any line blanketing. In this way, it seems that the most relevant spectral lines had been already included in the $1.7 \cdot 10^9$-lines ATLAS 8 ODFs of Kurucz (1979). The enhancement due to the $58 \cdot 10^9$-lines ATLAS 9 ODFs of Kurucz (1993a) is modest, at least for ordinary B stars.

(*b)* The effect of *microturbulence* is very small, as expected from its modest amount of additional line blanketing. We see no significant influence on the temperature structure if $\xi$ is varied from $0 - 8\,{\rm km\,s^{-1}}$.

(*c)* The influence of *metallicity*, however, is significant (Fig. 2). Enhanced element abundances increase not only the line absorption but also the bound-free and free-free absorption. There is a raise in temperature (i.e., a backwarming effect) at optical depths $\log \tau = -2...0$ which is the most relevant region for line formation. This explicit dependence on metallicity is a very important point virtually unrecognized in past B-star studies (Kilian-Montenbruck et al. 1994; Kaufer et al. 1994; Smartt & Rolleston 1997) where only *solar*-abundance atmospheres are used for line analysis. In Sect. 6.2 we will show that this will indeed have a clear influence on the actual line profiles.

(*d)* The *choice of the frequency grid* has no visible impact on the atmospheric structure. The Kurucz ODFs come in two flavors, a BIG grid with 328 frequency points and a LITTLE one with 1 212 points. The only, but valuable effect is the increased resolution of the LITTLE grid when dealing with the emitted flux of an atmosphere. However, this is of no importance for the present study.

(*e)* The *number of iterations* necessary for the model to converge has to be 10 at least. We always used the maximum possible, i.e., 15 iterations.

### *4.3. Atmosphere grid*

In summary, it is necessary to include the metallicity of the atmosphere as independent variable in addition to effective temperature and gravity. To obtain a sufficient coverage of the relevant parameter space we computed a three-dimensional ATLAS 9 model grid in reasonable resolution:

| | |
|---|---|
| $T_{\rm eff} = 20\,000...35\,000\,{\rm K}$ | in 1 000-K steps |
| $\log g = 3.0...4.5$ | in 0.1-dex steps |
| $[{\rm M/H}] = -1.0... + 0.5$ | in 0.5-dex steps |

where [M/H] is the mean logarithmic metallicity relative to solar of the ODF in use. The relative abundances of the elements therein are kept solar. Progress in including non–solar-scaled element mixtures could be possible in the near future when atmospheres based on opacity-sampling (OS) methods as the ATLAS 12 version of Kurucz will be available. However, in their preliminary study Castelli & Kurucz (1994) found no significant differences in the analysis of the A0 V star Vega between the ATLAS 9 and ATLAS 12 approaches.

The further parameters were fixed at 15 iterations, 64 depth levels, depth range from $\log \tau = -5... + 4$, LITTLE frequency grid, and $\xi = 8\,{\rm km\,s^{-1}}$, respectively. As shown above, the choice of the microturbulence parameter entering the *atmosphere* is uncritical and has no significance for the microturbulence to be derived from line analysis in Sect. 7. The solar model grid can be seen from Fig. 5 on as black points.

## 5. Synthetic LTE spectra

Before we consider non-LTE line formation for selected spectral lines in Sect. 6 it is reasonable to perform the choice of these lines by means of LTE methods. The basic problem for a proper selection are the *temperature-dependent* line blends of different chemical elements. Due to the modest computer time in LTE it is much easier to calculate all eventually relevant spectral lines of various elements.

The focus of such a computation, therefore, is not a detailed determination of single line profiles but a possibly complete set of lines taken into account. These requirements are met by the recent spectral-line list of Kurucz & Bell (1995) updating the classical list of Kurucz & Peytremann (1975). It includes wavelengths, oscillator strengths, and excitation energies of 530 000 atomic lines from the UV to the IR.

To obtain a series of representative spectra for B main-sequence stars we computed a set of 6 synthetic spectra between $T_{\rm eff} = 10\,000 - 35\,000$ K in 5 000-K steps using the Kurucz ATLAS 9 atmospheres together with a modified version of BHT (Baschek et al. 1966; Peytremann et al. 1967) LTE line formation, which allows the spectral synthesis of large spectral ranges. This code was also used in our previous work (Kaufer et al. 1994). Fixed input parameters for ATLAS 9 were $\log g = 4.0$ and solar metallicity. Within BHT we chose a broad wavelength range $\lambda = 3\,000 - 10\,000$ Å, a resolution $\Delta\lambda = 0.1$ Å, microturbulence $\xi = 10\,{\rm km\,s^{-1}}$, and a rotational profile of $v \sin i = 40\,{\rm km\,s^{-1}}$. *All* spectral lines of Kurucz & Bell (1995) were included in the computation. A search in the six 6 synthetic spectra (corresponding to spectral types O9 V–A0 V) for lines with $W_\lambda > 1$ mÅ yielded the following ions:

H I, He I/II, C I/II/III/IV, N I/II/III/IV, O I/II/III, Ne I/II/III, Na I/II, Mg I/II, Al I/II/III, Si I/II/III/IV, S I/II/III/IV, Cl I/II/III/IV, Ar I/II/III/IV, K I/II, Ca I/II/III, Sc II, Ti I/II/III/IV, V II, Cr I/II/III, Mn I/II/III, Fe I/II/III/IV, Co I/II, Ni I/II/III/IV, Cu I.

In order to make these synthetic spectra available to the public we designed a World Wide Web (WWW) interface, where any user can obtain a B-star spectrum by selecting one of the 6 temperatures and an arbitrary wavelength range between 3 000 and 10 000 Å (Gummersbach & Kaufer 1996). Further details are found at our WWW page.

**Table 2.** Undisturbed O II lines between 4 000 and 5 000 Å suitable for line analysis as function of effective temperature (or spectral type)

| Line | $T_{\rm eff}$ [K] | Line | $T_{\rm eff}$ [K] |
|---|---|---|---|
| O II 4185 | 32 500 – 22 500 | O II 4699 | 35 000 – 17 500 |
| O II 4415 | 35 000 – 17 500 | O II 4705 | 35 000 – 17 500 |
| O II 4452 | 27 500 – 17 500 | O II 4742 | 32 500 – 22 500 |
| O II 4591 | 35 000 – 22 500 | O II 4907 | 35 000 – 22 500 |
| O II 4596 | 35 000 – 17 500 | O II 4941 | 35 000 – 27 500 |
| O II 4662 | 35 000 – 22 500 | O II 4943 | 35 000 – 27 500 |
| O II 4696 | 32 500 – 22 500 | O II 4956 | 35 000 – 22 500 |

The main advantages of these spectra are *(a)* the explicit giving of the equivalent widths of all components in line blends, *(b)* the use as template spectra for radial-velocity determinations, *(c)* the use as reference spectra for line-free spectral regions to fix the continuum level, and *(d)* the possibility of a temperature-dependent selection of undisturbed lines of interest.

In this way, we performed an evaluation of all spectral lines between 3 800 and 5 200 Å corresponding to our observed spectra (Sect. 8), as function of effective temperature. In Sect. 7 we will see that the actual stellar-parameter analysis is determined mainly by Balmer, Si III/IV, and O II lines. Whereas there are only few Si lines suitable at all, there are numerous O II lines available. For these, we derived the most suitable ones as function of temperature (Table 2).

## 6. DETAIL/SURFACE non-LTE line formation

### 6.1. Implementation

The non-LTE line-formation program DETAIL/SURFACE (Giddings 1981; Butler & Giddings 1985; Butler 1984, 1994) solves the rate equations of statistical equilibrium and the radiation-transfer equation for a general model atom. DETAIL calculates the relevant occupation numbers which are passed to SURFACE to derive the synthetic spectrum. In our work we use the DETAIL version of Butler (1996) which, in addition to Butler (1994), takes advantage of accelerated lambda iteration (ALI) operators. The actual SURFACE version is from Becker (1997). The atomic data and oscillator strengths were taken from the CCP7 server (Jeffery 1993, 1996). Quoting the original sources, the data comprises model atoms of H I + He I/II (Husfeld 1996), C II (Eber & Butler 1988), N II (Becker & Butler 1988c, 1989), O II (Becker & Butler 1988ab), Mg II, Al III, and Si II/III/IV (Becker & Butler 1990ab).

The input for DETAIL is given by the ATLAS 9 atmospheres of Sect. 4.3, consisting of the mass integral, temperature, ion number density, and electron number density for each depth level of the corresponding atmosphere.

### 6.2. Parameter study

Similar to the ATLAS atmospheres (Sect. 4.2), we conduct a parameter study which illustrates the dependencies of the computed line profiles on *(a)* the parameters of the input ATLAS 9 atmosphere ($T_{\rm eff}$, $\log g$, [M/H]) and *(b)* the further parameters entering the problem from non-LTE line formation ($\xi_{\rm line}$, element abundance, $v \sin i$, LTE/non-LTE, number of iterations).

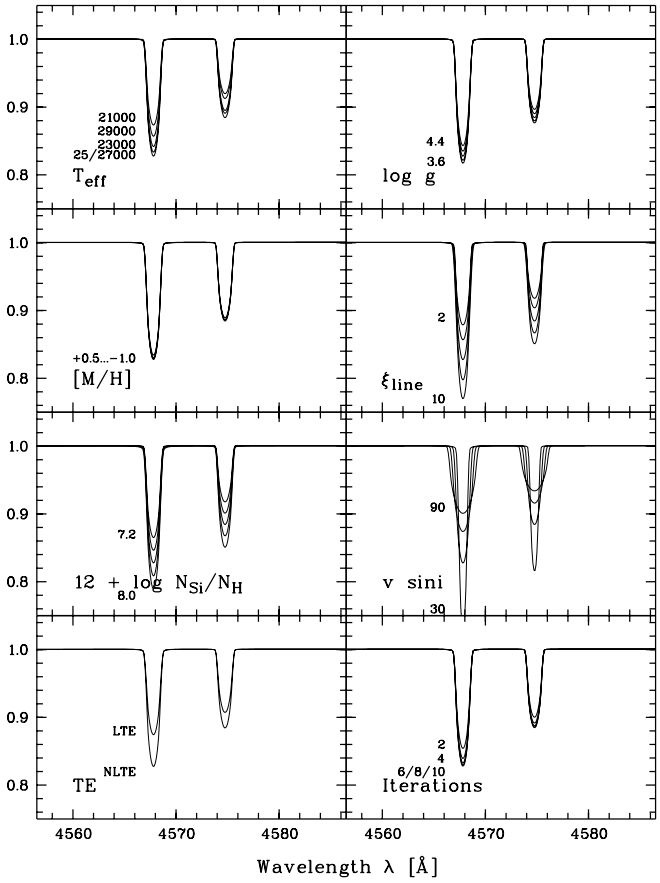


**Fig. 3.** Normalized non-LTE Si III 4568/75 profiles as function of temperature, gravity, atmosphere metallicity, line microturbulence, Si abundance, rotational velocity, LTE/non-LTE, and number of iterations in the DETAIL/SURFACE line computation. If not varied, $T_{\rm eff} = 25\,000$ K, $\log g = 4.0$, [M/H] = 0, $\xi_{\rm line} = 6$ km s$^{-1}$, $X_{\rm Si} = 7.6$, $v \sin i = 50$ km s$^{-1}$, non-LTE, and 10 iterations.

Figs. 3 and 4 shows the influence of each of these parameters on some of the strategic lines which will be used in the analysis in Sect. 7, Si III 4568/75 and O II 4591/96. Starting from a typical B-star model of $T_{\rm eff} = 25\,000$ K and $\log g = 4.0$ with solar abundances each parameter is varied while the others stay fixed. Whereas the behavior of $T_{\rm eff}$, $\log g$, element abundance, and $v \sin i$ is obvious and the number of iterations is uncritical, the effect of both the metallicity [M/H] of the atmosphere and the non-LTE is worth discussing.

*(a)* Surprisingly at first inspection, the O II lines (Fig. 4) seem to depend on *atmospheric metallicity*, whereas the Si III lines (Fig. 3) do not. In order to clarify this point we investigated this behavior as function of the full $T_{\rm eff}$-$\log g$ plane. Fig. 5 (*top*) shows the ratio of the equivalent widths of both O II 4591 and Si III 4568 calculated with 1/10-solar relative to solar metallicity. Here, the special cases of Figs. 3 and 4 are reproduced at $T_{\rm eff} = 25\,000$ K and $\log g = 4.0$.

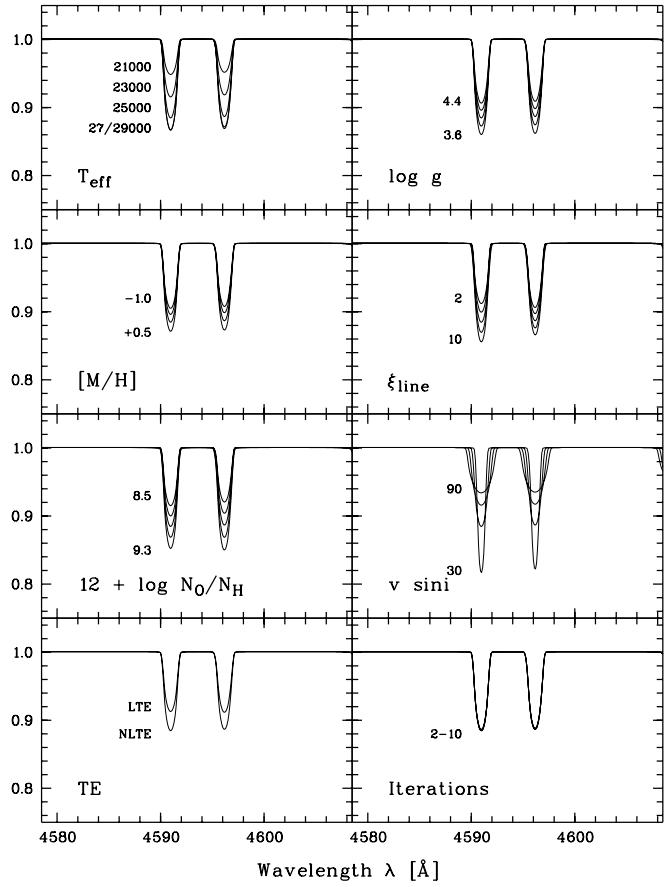


**Fig. 4.** Same as Fig. 3, for O II 4591/96 and $X_{\rm O} = 8.9$. Note the different behavior of [M/H].

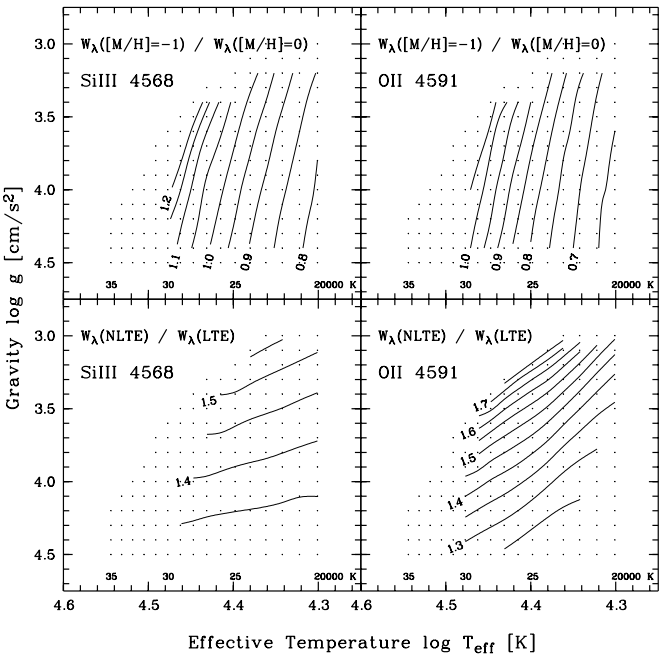


**Fig. 5.** *Top:* Effect of metallicity of the atmosphere $W_\lambda$([M/H]=-1)/$W_\lambda$([M/H]=0) as function of $T_{\rm eff}$ and $\log g$ for Si III 4568 and O II 4591 (cf. "[M/H]" in Figs. 3 and 4). *Bottom:* Non-LTE effect $W_\lambda$(non-LTE)/$W_\lambda$(LTE) (cf. "TE" in Figs. 3 and 4). The other parameters are held fixed as in Figs. 3 and 4. Black points denote the ATLAS 9 model grid of Sect. 4.3.

Now the dependence of a spectral line on the metallicity of the atmosphere can easily be explained. As shown by the backwarming effect in Fig. 2, an increase in metallicity acts like an increase in effective temperature, i.e., it raises the temperature structure of the atmosphere. Therefore, the strength of a given metal line in a outwards cooling photosphere (cf. Figs. 1, 2) is modified by metallicity in the way that *increased metallicity strengthens the line if $T_{\rm eff}$ is below the temperature of maximum line strength, and weakens the line if $T_{\rm eff}$ is above the temperature of maximum line strength*.

These well-known maxima arising from the excitation-ionization equilibrium are traced by the "1.0" curves in Fig. 5. In this way, the independence of the Si III line in Fig. 3 on metallicity derives from its vicinity to the line-strength maximum of Si III, which is near $T_{\rm eff} = 26\,000$ K at $\log g = 4$ (cf. Fig. 6). Conversely, this is not the case for the O II line (Fig. 4) the maximum of which for $\log g = 4$ is located near $T_{\rm eff} = 28\,500$ K. *The influence of the metallicity of the atmosphere on metal lines is strong if the lines are temperature-sensitive.*

If the consistency between the abundance from line analysis and the atmospheric abundance is neglected, errors of several tenths of dex in the abundance determination arise as soon as the effective temperature of the star departs several thousand degrees from the temperature of the line-strength maximum of the spectral line in use. Since B-star analyses generally invoke line strengths of O II and Si lines of various ionization stages there is no single temperature ever fitting the line-strength maxima of all these species simultaneously. That means that this problem naturally occurs if stars of non-solar abundances are analyzed by means of model atmospheres with solar abundances. As shown in the following sections, this point is of prime importance for a proper determination of possible deviations from solar abundance patterns in the Galactic disk.

*(b)* Similarly, we plotted the *non-LTE effect* of Figs. 3 and 4 as function of $T_{\rm eff}$ and $\log g$ (Fig. 5, *bottom*). The ratio between non-LTE and LTE increases with increasing $T_{\rm eff}$ but mainly with decreasing $\log g$. The curves of equal non-LTE/LTE ratio run approximately parallel to the limit of stable ATLAS models and therefore about parallel to the Eddington limit. Qualitatively, the falling gas pressure and density with decreasing $\log g$ supports the transition from a collision-dominated to a radiation-dominated gas and the corresponding departures from thermodynamic equilibrium.

### 6.3. Spectral-line grid

Keeping the results of the past section in mind we calculated a detailed model grid of synthetic non-LTE spectra of the ions relevant for line analysis—H I, O II, and Si II/III/IV. Due to the computational effort it is presently not possible to take several ions into account simultaneously (Butler, priv. comm.), as we

**Table 3.** Concordance between atmosphere abundance and line abundance used in the computed O and Si model grids. The solar abundances $X_{\mathrm{O},\odot} = 8.9$ and $X_{\mathrm{Si},\odot} = 7.6$ are adopted from Grevesse et al. (1996).

| [M/H] | $X_{\mathrm{O}} = 12 + \log(N_{\mathrm{O}}/N_{\mathrm{H}})$ | $X_{\mathrm{Si}} = 12 + \log(N_{\mathrm{Si}}/N_{\mathrm{H}})$ |
|---|---|---|
| $-1.0$ | 7.9 | 6.6 |
| $-0.5$ | 8.4 | 7.1 |
| 0.0 | 8.9 | 7.6 |
| $+0.5$ | 9.4 | 8.1 |

did with the LTE spectrum synthesis in Sect. 5. Instead, the non-LTE spectra are mostly computed for each ion separately. Starting point is the 3-dimensional ATLAS 9 $T_{\mathrm{eff}}$-$\log g$-[M/H] atmosphere grid (Sect. 4.3).

*(a) Hydrogen grid.* As hydrogen lines do not depend on microturbulence and formal abundance the calculation is straightforward. Since we are going to use H$\gamma$ for analysis in Sect. 7.1 we extracted the surroundings of H$\gamma$ from the total spectrum (which in this case is a spectrum synthesis of H I, He I, and He II lines) and convolved it with a rotational velocity $v \sin i = 5 - 100\,\mathrm{km\,s^{-1}}$ in 5-$\mathrm{km\,s^{-1}}$ steps. From these spectra we extracted the right half-profile of H$\gamma$, which will be used for the actual analysis in Sect. 7.1. In summary, we obtained a 4-dimensional $T_{\mathrm{eff}}$-$\log g$-[M/H]-$v \sin i$ line-profile grid for H$\gamma$.

*(b) Oxygen grid.* As we want to measure only equivalent widths for metal lines and to ignore their actual profiles (Sect. 7.3) $v \sin i$ can be ignored at the moment. We computed O II spectra with a microturbulence $\xi = 0 - 12\,\mathrm{km\,s^{-1}}$ in 2-$\mathrm{km\,s^{-1}}$ steps. In order to maintain the concordance between atmosphere abundance and line abundance pointed out in Sect. 6.2 we used only those O abundances $X_{\mathrm{O}}$ which fitted the four ATLAS 9 ODF metallicities [M/H] (Table 3). From the resulting O II spectra we integrated the equivalent widths of the O II lines given in Table 2. Only at this point we entered the actual O abundance $X_{\mathrm{O}} = 7.9 - 9.4$ in 0.1-dex steps. This was done by a logarithmic cubic-spline interpolation of the four equivalent widths for [M/H]=-1.0, -0.5, 0.0, and +0.5 between $X_{\mathrm{O}} = 7.9 - 9.4$ for a given $T_{\mathrm{eff}}$, $\log g$, and $\xi$. In this way, the problem of abundance inconsistency could be explicitly avoided. In summary, we obtained a 4-dimensional $T_{\mathrm{eff}}$-$\log g$-$X_{\mathrm{O}}$-$\xi$ equivalent-width grid for each O II line.

*(c) Silicon grid.* Quite analogously, we computed the corresponding Si II/III/IV grid. The integrated lines are Si II 5041, 5056; Si III 4553, 4568, 4575, 4717, 4813, 4820, 4829; and Si IV 4116, 4212, 4631, 4654. In accordance to Table 3 a Si abundance $X_{\mathrm{Si}} = 6.6 - 8.1$ in 0.1-dex steps was used for interpolation. The range of microturbulence was the same as above. In summary, we obtained a 4-dimensional $T_{\mathrm{eff}}$-$\log g$-$X_{\mathrm{Si}}$-$\xi$ equivalent-width grid for each Si line.

For the other ions (He I/II, C II, N II, Mg II, and Al III) no dedicated model grids were computed because they do not directly enter the determination of stellar parameters. Their abundances will be obtained once the stellar parameters have been derived from H I, O II, and Si II/III/IV lines (Sect. 7.4).

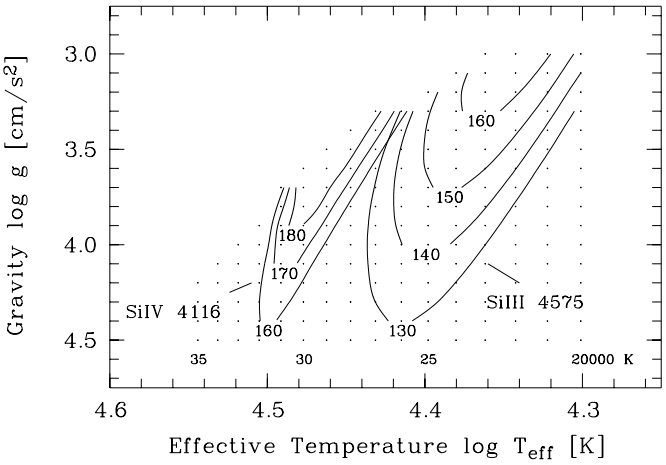


**Fig. 6.** Curves of equal equivalent widths $W_\lambda$ [mÅ] of Si IV 4116 and Si III 4575 for $\xi = 6\,\mathrm{km\,s^{-1}}$ and $X_{\mathrm{Si}} = 7.6$ as function of $T_{\mathrm{eff}}$ and $\log g$ derived from the theoretical non-LTE Si grid of Sect. 6.3.

## 7. Method of analysis

Chemical analyses of B stars near the main sequence are based on the application of three physical conditions constraining the stellar parameters: *(a)* the independence of Balmer lines of microturbulence and abundance *(b)* the ionization equilibrium of the Si II/III/IV lines and *(c)* the microturbulence condition, which states that both weak and strong O II lines must yield the same O abundance.

Most authors offer the Balmer analysis in a $T_{\mathrm{eff}}$-$\log g$, the Si analysis in a $T_{\mathrm{eff}}$-$X_{\mathrm{Si}}$, and the O analysis in a $W_\lambda$-$X_{\mathrm{O}}$ diagram (e.g. Kaufer et al. 1994). However, in this way all these analyses depend on the former. Systematic errors can propagate from one analysis to the next. The very influence of a single input parameter is hard to trace across the H, Si, and O analyses. In the present work, we adopt a slightly different approach. We will analyze the H, Si, and O lines *separately* and join the single analyses together in one overall analysis in a $\log T_{\mathrm{eff}}$-$\log g$ diagram in Sect. 7.4.

### *7.1. Hydrogen analysis*

Since we will mainly deal with observed spectra in the region 4 000–5 000 Å (Sect. 8) the Balmer lines H$\beta$-H$\delta$ are at disposal for hydrogen analysis. Between $T_{\mathrm{eff}} = 20\,000 - 30\,000$ K the H$\beta$ profile is less affected by O II lines than the other Balmer lines (notably the red wing of H$\delta$) but often suffers severe absorption by the diffuse interstellar band (DIB) at 4 882 Å. In addition, it might be dangerous for analyses with LTE atmospheres to use lower Balmer lines like H$\alpha$ or H$\beta$ which originate far out in the atmosphere where possible non-LTE effects could affect the temperature structure. As a reasonable compromise we chose H$\gamma$ the blue wing of which is generally very undisturbed. In detail, we performed the following steps in analyzing the Balmer lines.

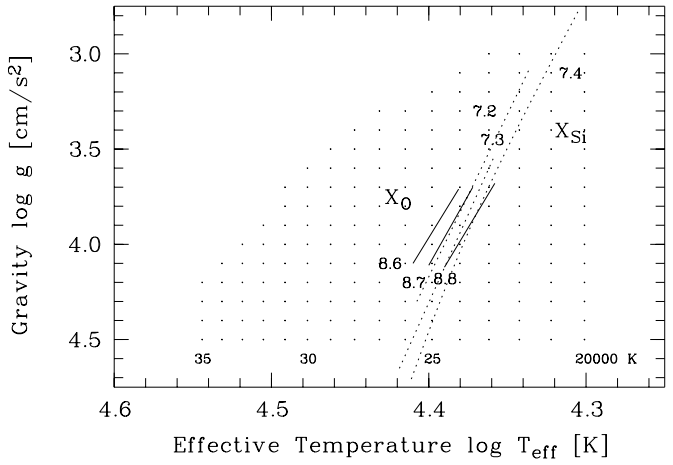


**Fig. 7.** Curves minimizing the difference between observed and synthetic non-LTE Si III/IV (*dotted*) and O II equivalent widths (*solid*) as function of $X_{\rm Si} = 7.2 - 7.4$ and $X_{\rm O} = 8.6 - 8.8$, respectively, for SH 2-208/6 as example.

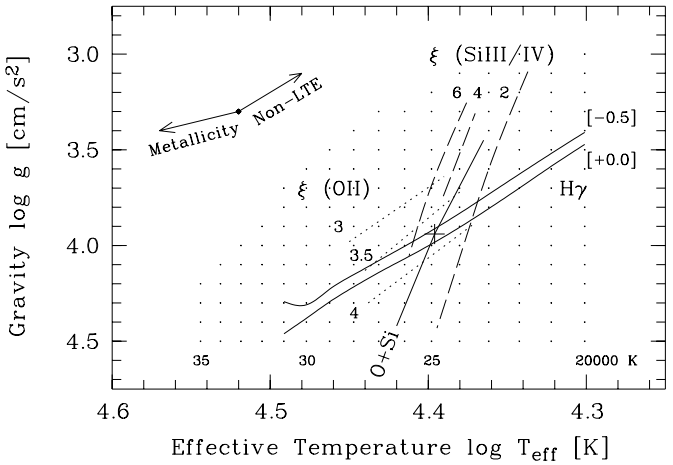


**Fig. 8.** Overall analysis: Hydrogen analysis as function of [M/H]=0 and -0.5 (*solid*), silicon analysis as function of $\xi$ (*dashed*), oxygen analysis as function of $\xi$ (*dotted*), combined silicon and oxygen analysis (*solid*), and the derived stellar parameters (+) for SH 2-208/6. The arrows denote the metallicity effect of sub-solar atmospheres and the non-LTE effect discussed in Sect. 9.

*(a) Check of wavelength calibration.* The observed spectra is shifted in order to fit exactly the H$\gamma$ wavelength of 4 340.46 Å used in line-formation calculations.

*(b) Check of flux normalization.* To correct for potential echelle-reduction problems we renormalize the H$\gamma$ region by using the line-free regions (according to the synthetic LTE spectra of Sect. 5) at $\lambda = 4\,298 - 4\,302$ Å and $\lambda = 4\,397 - 4\,403$ Å as true continuum.

*(c) Mirroring of line wings.* To extract the available information of *both* line wings we mirror the line profile at its symmetry axis. In this way, we are able to subtract the O II-line absorption and to recover the pure Balmer profile.

*(d) Extraction of corrected line profile.* We extract the red wing of this recovered H$\gamma$ profile in the range 0-20 Å relative to the line center. This corresponds to the theoretical non-LTE H$\gamma$ profiles calculated in Sect. 6.3.

*(e) Variance analysis.* An analysis of variance

$$\sigma^2 = \sum_{\lambda=4\,340.46}^{4\,360.46} \left(f_{\lambda,\rm th} - f_{\lambda,\rm obs}\right)^2, \quad \Delta\lambda = 0.01 \text{ Å}$$

is performed for the observed half-profile $f_{\lambda,\rm obs}$ and each calculated theoretical profile $f_{\lambda,\rm th}$ in the $T_{\rm eff}$-$\log g$-[M/H]-$v \sin i$ parameter space. Minimizing $\sigma^2$ for each $T_{\rm eff}$ leads to best-fit hydrogen curves for each [M/H] in the $T_{\rm eff}$-$\log g$ diagram (solid lines in Fig. 8), which reflect the well-known $T_{\rm eff}$-$\log g$ degeneracy of Balmer-line profiles.

It is important here to realize that there is a significant dependence of Balmer lines on the metallicity [M/H] of their atmosphere. The reason is essentially the same already stated for the metal lines in Sect. 6.2 (Figs. 4, 5). Enhanced atmospheric metallicity mimicking increased effective temperature lowers the equivalent widths for B stars because the line-strength maximum for hydrogen occurs at A stars. Therefore, for increased [M/H] a given $W_\lambda$ is reached at lower $T_{\rm eff}$ (Fig. 8).

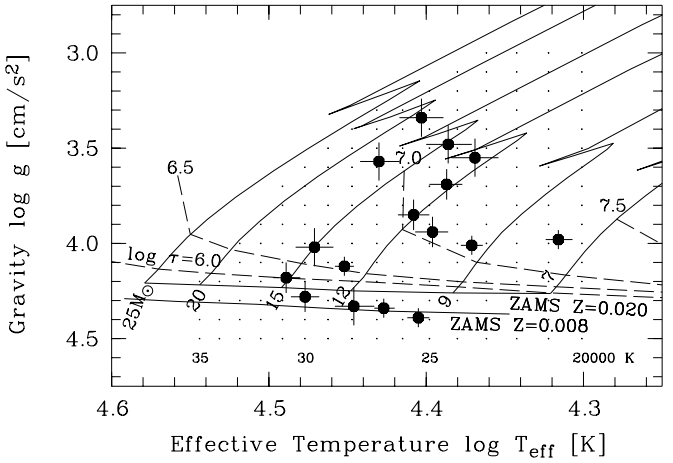


**Fig. 9.** Location of the observational sample in the $\log T_{\rm eff}$-$\log g$ diagram. Solar evolutionary tracks (*solid*), solar and sub-solar zero-age main sequences (ZAMS) (*solid*), and solar isochrones (*dashed*) derived from $Z = 0.020$ (Schaller et al. 1992) and $Z = 0.008$ data (Schaerer et al. 1993) are shown. Accounting for lower metallicities than solar, all stars of the sample are perfectly confined to the main sequence predicted by stellar-evolution theory, i.e., to the core hydrogen-burning phase of their evolution.

We determined the influence of $v \sin i$ on the hydrogen fit curves to be very moderate. Actually, the curves for 10 and 100 $\rm km\,s^{-1}$ are almost indistinguishable. Obviously, the rotational broadening for $v \sin i < 100 \rm\ km\,s^{-1}$ is restricted to very line core, which is far less important than the evident dependence of the Balmer wings on $T_{\rm eff}$ and $\log g$. This, in turn, exclude the Balmer lines from any attempt to derive $v \sin i$.

### *7.2. Silicon analysis*

From the non-LTE silicon model grid (Sect. 6.3) one can derive curves of constant equivalent width in the $T_{\rm eff}$-$\log g$-$X_{\rm Si}$-$\xi$ parameter space. Fig. 6 shows these curves for Si IV 4116 and Si III 4575 with $X_{\rm Si} = 7.6$ and $\xi = 6\,{\rm km\,s^{-1}}$ as example. The location of the relevant line-strength maxima is clearly visible (cf. the 1.0 curve of Si III 4568 in Fig. 5). Ionization equilibrium of Si III/IV now demands that the curves corresponding to the observed equivalent widths are intersecting in one point, given a fixed $X_{\rm Si}$ and $\xi$. Incorporating one of the two remaining parameters, connections of these intersection points in the $T_{\rm eff}$-$\log g$ diagram can be obtained as function of either $X_{\rm Si}$ or $\xi$. Reasonably, we choose the $\xi$ dependence to determine the stellar parameters because this dependence is shared by the O II lines. The resulting Si curves as function of $\xi = 2 - 4\,{\rm km\,s^{-1}}$ are shown in Fig. 8 (dashed lines). Equivalently, the Si curves as function of $X_{\rm Si}$ are shown in Fig. 7 (dotted lines). They will be used to derive the Si abundance once the stellar parameters will be determined. Note that a given ($T_{\rm eff}$, $\log g$, $\xi$) will uniquely fix $X_{\rm Si}$, and a given ($T_{\rm eff}$, $\log g$, $X_{\rm Si}$) will fix $\xi$, analogously.

### *7.3. Oxygen analysis*

For the oxygen analysis we used the O II lines given in Table 2, according to the relevant temperature range. Traditionally, microturbulence is derived by a large number of weak and strong O lines. In the present work, we restricted the number of lines to about 5–10 in favor of being actually undisturbed by lines of other ions. From the non-LTE oxygen model grid (Sect. 6.3) we derive the microturbulence for each $T_{\rm eff}$-$\log g$ point, which minimizes the sum of the squared departures of the observed line widths (of different size) from the theoretical ones, covering the complete O-abundance range of the model grid. These $\xi$s as function of $T_{\rm eff}$ and $\log g$ are shown in Fig. 8 (dotted lines). This method is completely equivalent to the canonical $\xi$ determination from a $W_\lambda$-$X_{\rm O}$ diagram with a horizontal linear regression. Analogously to the Si analysis above, the O abundance can be given as function of $X_{\rm O}$, as well (Fig. 7, solid lines).

### *7.4. Overall analysis*

At this point, we have gathered all three analyses—hydrogen, silicon, and oxygen—in the $T_{\rm eff}$-$\log g$ diagram for the overall analysis (Fig. 8). The determination of stellar parameters now proceeds as follows.

*(a) Intersection of Si and O analyses.* The curves of equal microturbulence of Si and O are intersected yielding the solid line labeled "O+Si" in Fig. 8. In this way, the microturbulence information of both oxygen *and* silicon lines are consistently taken into account, contrary to prior B-star analyses met in the literature.

*(b) Intersection of Si/O and H analyses.* The crossing of the Si/O curve and the Balmer curve at this moment depends on the unknown metallicity [M/H]. Note that by the abundance-consistent derivation of the Si and O model grids (Table 3) their metallicity dependence had been already implicitly taken into account. The small remaining $T_{\rm eff}$-$\log g$ range in which the Si/O curve intersects the two H$\gamma$ curves is now compared with the Si and O abundances (Fig. 7) in the same range. The mean of these Si and O abundances relative to solar ([M/H]$\approx -0.3$ in Fig. 8) is then transferred to the Balmer analysis. Taken at face value, this step would require the Si and O abundances, relative to solar, to be fully representative for all metals. However, keep in mind that we are dealing with a final adjustment of some hundred degrees in effective temperature or about 0.1 dex in gravity. The uncertainty of this adjustion is even smaller.

At this point, we consistently determine the stellar parameters $T_{\rm eff}$, $\log g$, and $\xi$, and the chemical abundances $X_{\rm Si}$ and $X_{\rm O}$ of the star in consideration ("+" in Fig. 8). The error of the parameter determination mainly arise from the error of the measured equivalent widths and line profiles. This uncertainty is about 10% in $W_\lambda$ for a signal-to-noise ratio $S/N = 100$. Performing the analysis by using an equivalent width increased/decreased by $\pm 10\%$ corresponds to an error of 500 K in $T_{\rm eff}$, 0.1 dex in $\log g$, 1 km/s in $\xi$, and 0.1 dex in the Si and O abundances.

*(c) Calculation of the actual stellar model.* Using the derived stellar parameters we compute an ATLAS 9 atmosphere (cf. Sect. 4). Since the ATLAS ODFs are only available in 0.5-dex steps in metallicity we actually compute two ATLAS models adjacent in metallicity and interpolate the resulting atmosphere structures according to the derived Si/O metallicity. This atmosphere is passed to DETAIL/SURFACE which computes the corresponding synthetic non-LTE Si and O spectra (cf. Sect. 6).

*(d) Determination of $v \sin i$.* The Si and O spectra are convolved with rotational profiles of $v \sin i = 0 - 100\,{\rm km\,s^{-1}}$ in 5-${\rm km\,s^{-1}}$ steps. The rotational velocity is now derived by fitting the observed Si III 4568/75 and O II 4591/96 lines (cf. Figs. 3, 4) which had be previously been used to determine the stellar parameters, as well.

*(e) Determination of the additional metal abundances.* Using the derived $v \sin i$ we compute synthetic non-LTE spectra of He I/II, C II, N II, Mg II, and Al III as function of the corresponding metal abundance in 0.1-dex steps. By fitting trustworthy spectral lines, selected in an analogous way like the Si and O lines with the synthetic LTE spectra (Sect. 5) — mainly He I 4713, C II 4619, N II 4237/42, Mg II 4481, and Al III 4150/4480 — we determine the relevant abundances.

*(f) Visual inspection of the spectral-line fits.* Finally, an visual check is performed whether the computed non-LTE spectra of different ions actually fit the observed spectrum for the derived set of parameters (Fig. 10).

## 8. Observational sample of B stars and results

### *8.1. Selection of B stars*

We apply the method of analysis outlined in the past section to our observed sample of B stars in the Galactic disk (Table 4). Part of the objects ($R_{\rm GC} > 8{\rm kpc}$) are from Kaufer et al. (1994). Generally, we changed the object identifiers to the standard SIMBAD

**Table 4.** Observational sample of Galactic B stars. Objects with $R_{\rm GC} > 8$ kpc are from Kaufer et al. (1994). SH = *Sharpless*, NGC = *New General Catalogue*, Cl = *Cluster*, HR = *Harvard Revised*, ESO = *European Southern Observatory*, CA = *Calar Alto*, CASPEC = *Cassegrain Echelle Spectrograph*, FLASH = *Fiber Linked Astro Echelle Spectrograph Heidelberg*.

| Object | Date | Telescope | Instrument | Observer | $V$ [mag] | $t_{\rm exp}$ [min] | $S/N$ | $\lambda$ [Å] | $\lambda/\Delta\lambda$ | $R_{\rm GC}$ [kpc] |
|---|---|---|---|---|---|---|---|---|---|---|
| SH 2-47/3 | 94/04 | ESO 3.6-m | CASPEC | Szeifert | 10.30 | 30 | 80 | 3 800–5 200 | 18 000 | 5.6 |
| NGC 6611/150 | 94/04 | ESO 3.6-m | CASPEC | Szeifert | 9.85 | 18 | 110 | 3 800–5 200 | 18 000 | 6.0 |
| Cl Hogg 22/5 | 94/04 | ESO 3.6-m | CASPEC | Szeifert | 10.47 | 15 | 100 | 3 800–5 200 | 18 000 | 6.0 |
| Cl Lynga 6/Q | 94/04 | ESO 3.6-m | CASPEC | Szeifert | 13.18 | 60 | 60 | 3 800–5 200 | 18 000 | 6.8 |
| Cl Pismis 20/6 | 94/04 | ESO 3.6-m | CASPEC | Szeifert | 11.91 | 60 | 65 | 3 800–5 200 | 18 000 | 7.0 |
| NGC 6823/E77 | 94/04 | ESO 3.6-m | CASPEC | Szeifert | 10.40 | 20 | 95 | 3 800–5 200 | 18 000 | 7.6 |
| HR 1763 | 90/09 | CA 2.2-m | FLASH | Krenzin | 5.79 | 10 | 200 | 4 000–6 800 | 12 000 | 8.9 |
| HR 1765 | 90/09 | CA 2.2-m | FLASH | Krenzin | 4.72 | 10 | 400 | 4 000–6 800 | 12 000 | 8.9 |
| HR 1842 | 90/09 | CA 2.2-m | FLASH | Krenzin | 5.46 | 10 | 200 | 4 000–6 800 | 12 000 | 8.9 |
| HR 1886 | 90/09 | CA 2.2-m | FLASH | Krenzin | 5.67 | 10 | 200 | 4 000–6 800 | 12 000 | 8.9 |
| HR 1887 | 90/09 | CA 2.2-m | FLASH | Krenzin | 4.78 | 10 | 200 | 4 000–6 800 | 12 000 | 8.9 |
| h Per/717 | 90/09 | CA 2.2-m | FLASH | Krenzin | 9.28 | 120 | 80 | 4 000–6 800 | 12 000 | 10.3 |
| h Per/782 | 90/09 | CA 2.2-m | FLASH | Krenzin | 9.45 | 180 | 80 | 4 000–6 800 | 12 000 | 10.3 |
| SH 2-208/6 | 92/12 | CA 3.5-m | Twin | Kaufer | 12.65 | 60 | 150 | 4 000–5 080 | 6 000 | 11.6 |
| SH 2-247/1 | 92/12 | CA 3.5-m | Twin | Kaufer | 11.07 | 60 | 250 | 4 000–5 080 | 6 000 | 12.0 |
| SH 2-217/3 | 92/12 | CA 3.5-m | Twin | Kaufer | 11.34 | 60 | 200 | 4 000–5 080 | 6 000 | 13.5 |

**Table 5.** Stellar parameters and chemical abundances of the observational sample derived from non-LTE line analysis. $X_i \equiv 12 + \log(N_i/N_{\rm H})$, solar abundances ($\odot$) from Grevesse et al. (1996), spectral types corresponding to $T_{\rm eff}$ according to Humphreys & McElroy (1984), masses and ages from stellar evolutionary tracks of solar and sub-solar metallicities (Schaller et al. 1992; Schaerer et al. 1993).

| Object | $T_{\rm eff}$ [K] | $\log g$ | $\xi$ [km/s] | $v \sin i$ [km/s] | $X_{\rm He}$ | $X_{\rm C}$ | $X_{\rm N}$ | $X_{\rm O}$ | $X_{\rm Mg}$ | $X_{\rm Al}$ | $X_{\rm Si}$ | Type | $M_{\rm evol}$ [$M_\odot$] | $\log \tau_{\rm evol}$ [yr] |
|---|---|---|---|---|---|---|---|---|---|---|---|---|---|---|
| $\odot$ | | | | | *10.99* | *8.55* | *7.97* | *8.87* | *7.58* | *6.49* | *7.56* | | | |
| SH 2-47/3 | 29 600 | 4.02 | 4 | 20 | 11.30 | 8.10 | 7.70 | 8.51 | 7.40 | 6.10 | 7.40 | B0 V | 15.0 | 6.65 |
| +/- | *800* | *0.10* | *1* | *15* | *0.30* | *0.15* | *0.10* | *0.10* | *0.15* | *0.15* | *0.10* | | *0.5* | *0.15* |
| NGC 6611/150 | 27 900 | 4.33 | 6 | 80 | 10.90 | 8.30 | 7.80 | 8.63 | 7.60 | | 7.40 | B0.2 V | 11.5 | <6.00 |
| +/- | *800* | *0.10* | *2* | *15* | *0.30* | *0.15* | *0.10* | *0.10* | *0.15* | | *0.10* | | *0.5* | |
| Cl Hogg 22/5 | 26 900 | 3.57 | 4 | 40 | 11.40 | 8.40 | 8.00 | 8.64 | 7.80 | 6.80 | 8.20 | B0.2 V | 17.0 | 6.95 |
| +/- | *800* | *0.10* | *2* | *15* | *0.30* | *0.20* | *0.15* | *0.10* | *0.15* | *0.15* | *0.10* | | *1.0* | *0.10* |
| Cl Lynga 6/Q | 23 400 | 3.55 | 6 | 40 | 11.10 | 8.30 | 8.20 | 8.87 | 7.60 | 6.20 | 7.29 | B1 III | 12.5 | 7.20 |
| +/- | *800* | *0.10* | *2* | *15* | *0.30* | *0.20* | *0.20* | *0.10* | *0.15* | *0.15* | *0.10* | | *1.5* | *0.20* |
| Cl Pismis 20/6 | 25 300 | 3.34 | 5 | 45 | 11.50 | 8.30 | 8.20 | 8.80 | 7.70 | 6.60 | 7.92 | B0.5 III | 19.0 | 7.00 |
| +/- | *800* | *0.10* | *2* | *15* | *0.30* | *0.15* | *0.10* | *0.10* | *0.15* | *0.15* | *0.10* | | *3.0* | *0.20* |
| NGC 6823/E77 | 24 300 | 3.48 | 11 | 60 | 11.40 | 8.30 | 7.64 | 8.65 | 7.50 | 6.10 | 7.43 | B0.5 III | 15.0 | 7.15 |
| +/- | *800* | *0.10* | *2* | *15* | *0.30* | *0.15* | *0.10* | *0.10* | *0.15* | *0.15* | *0.10* | | *2.0* | *0.20* |
| HR 1763 | 26 700 | 4.34 | 2 | 50 | 11.10 | 8.20 | 7.88 | 8.70 | 7.70 | 6.30 | 7.53 | B0.5 V | 10.5 | <6.00 |
| +/- | *400* | *0.05* | *1* | *10* | *0.15* | *0.12* | *0.08* | *0.08* | *0.12* | *0.12* | *0.08* | | *0.5* | |
| HR 1765 | 23 500 | 4.01 | 1 | 25 | 11.10 | 8.20 | 7.40 | 8.20 | 8.00 | 6.15 | 7.08 | B1 V | 9.0 | 7.20 |
| +/- | *400* | *0.05* | *1* | *10* | *0.15* | *0.12* | *0.08* | *0.08* | *0.12* | *0.12* | *0.08* | | *0.5* | *0.10* |
| HR 1842 | 20 700 | 3.98 | 1 | 30 | 10.90 | 8.20 | 7.80 | 8.83 | 7.25 | 6.00 | 7.51 | B1.5 V | 8.0 | 7.25 |
| +/- | *400* | *0.05* | *1* | *10* | *0.30* | *0.12* | *0.08* | *0.08* | *0.12* | *0.12* | *0.08* | | *0.5* | *0.10* |
| HR 1886 | 25 400 | 4.39 | 2 | 30 | 11.10 | 8.20 | 7.72 | 8.75 | 7.80 | 6.40 | 7.49 | B1 V | 9.5 | <6.00 |
| +/- | *400* | *0.05* | *1* | *10* | *0.20* | *0.12* | *0.12* | *0.08* | *0.12* | *0.12* | *0.08* | | *0.5* | |
| HR 1887 | 28 300 | 4.12 | 6 | 40 | 11.30 | 8.00 | 7.58 | 8.61 | 7.45 | 6.25 | 7.51 | B0.2 V | 13.0 | 6.55 |
| +/- | *400* | *0.05* | *1* | *10* | *0.30* | *0.12* | *0.12* | *0.08* | *0.12* | *0.12* | *0.08* | | *0.5* | *0.10* |
| h Per/717 | 25 600 | 3.85 | 12 | 80 | 10.90 | | 7.50 | 8.48 | 7.40 | 6.00 | 7.22 | B0.5 V | 12.0 | 7.05 |
| +/- | *600* | *0.08* | *2* | *10* | *0.20* | | *0.15* | *0.10* | *0.15* | *0.15* | *0.10* | | *0.5* | *0.10* |
| h Per/782 | 24 400 | 3.69 | 4 | 50 | 10.90 | 8.10 | 7.60 | 8.54 | 7.50 | 6.10 | 7.23 | B0.5 V | 12.0 | 7.10 |
| +/- | *600* | *0.08* | *1* | *10* | *0.20* | *0.15* | *0.15* | *0.10* | *0.15* | *0.15* | *0.10* | | *0.5* | *0.10* |
| SH 2-208/6 | 24 900 | 3.94 | 4 | 25 | 10.90 | 8.20 | 7.77 | 8.65 | 7.08 | 6.10 | 7.05 | B0.5 V | 10.5 | 7.05 |
| +/- | *600* | *0.08* | *1* | *10* | *0.15* | *0.15* | *0.10* | *0.10* | *0.15* | *0.15* | *0.10* | | *0.5* | *0.10* |
| SH 2-247/1 | 30 800 | 4.18 | 11 | 40 | 11.00 | 8.00 | 7.50 | 8.28 | 7.10 | 6.20 | 7.07 | B0 V | 15.0 | 6.50 |
| +/- | *600* | *0.08* | *2* | *10* | *0.20* | *0.15* | *0.15* | *0.10* | *0.15* | *0.15* | *0.10* | | *0.5* | *0.10* |
| SH 2-217/3 | 30 000 | 4.28 | 13 | 60 | 10.80 | | 7.20 | 7.89 | 6.95 | 6.20 | 6.77 | B0 V | 13.0 | <6.00 |
| +/- | *600* | *0.08* | *2* | *10* | *0.20* | | *0.15* | *0.10* | *0.15* | *0.15* | *0.10* | | *1.0* | |

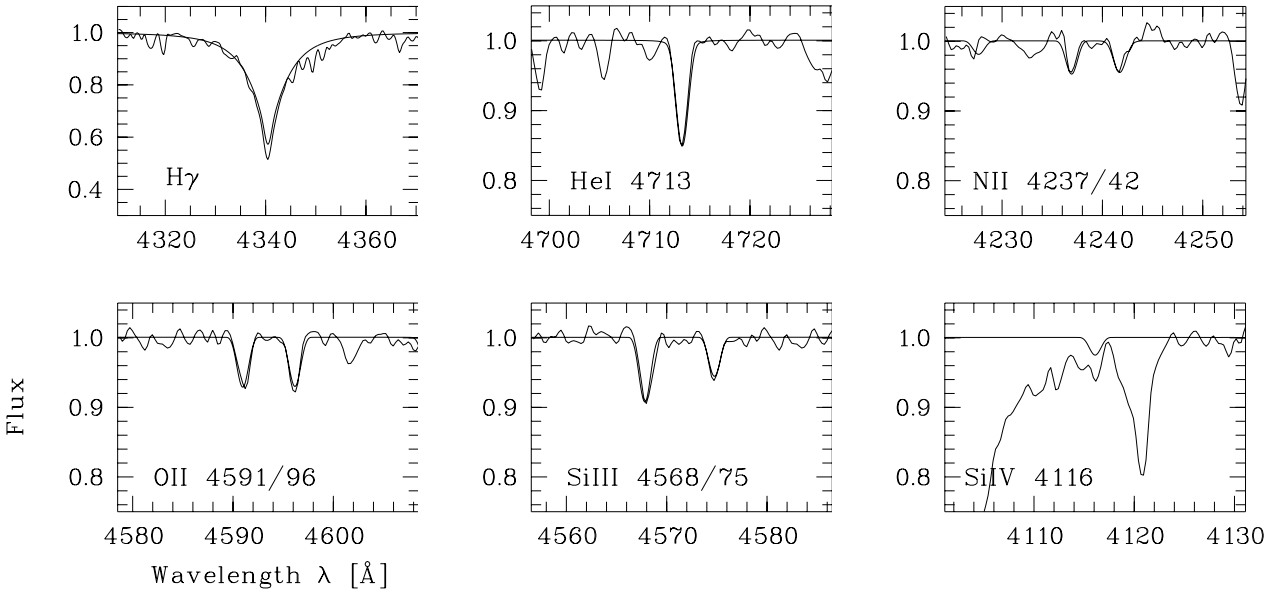


**Fig. 10.** Non-LTE profiles of strategic spectral lines of various ions calculated from the derived stellar parameters and abundances, confronted with the observed spectrum for SH 2-208/6. Note that the computed non-LTE profiles are single-ion spectra each, leaving the lines of other ions unconsidered (e.g. O II 4705/10 near He I 4713, or H$\delta$ 4102 and O II 4119/He I 4121 near Si IV 4116).

notation if necessary. For homogeneity reasons we disregarded the stars NGC 6531/2, NGC 6823/34, NGC 6910/2, NGC 1893/9, and NGC 1893/10 because the wavelength range of H$\gamma$, to be used in the analysis (Sect. 7.1), was not covered in their Coudé spectra. The analysis of SH 2-301/3 yielded no consistent results. The galactocentric distance of SH 2-208/6 is adopted from Smartt & Rolleston (1997). In sum, 10 objects from the Kaufer et al. (1994) sample are reanalyzed in the present study.

The remaining 6 objects ($R_{\rm GC} < 8$ kpc) are new observations carried out at the European Southern Observatory (ESO) 3.6-m telescope with the Cassegrain Echelle Spectrograph (CASPEC). The instrumental set-up consisted of the blue cross-disperser, the short camera and a Tek $512 \times 512$ CCD chip with 24-$\mu$m pixel size (Pasquini 1993). The objects had been selected by their extinction-free color index

$$Q = (U-B) - 0.72\,(B-V) \approx (-0.78 \pm 0.05)\,\mathrm{mag}$$

typical for B1 V main-sequence stars. Mid-resolution pre-observations were performed at the ESO 1.52-m telescope with the Boller & Chivens spectrograph in April 1994. Stars with strong rotationally broaded lines and stars with visible wind emission have been neglegted. In turn, the remaining objects were observed with CASPEC as described above. The $UBV$ data and distances are from Moffat & Vogt (1973, 1975) and Lahulla (1985). For a discussion of the relevant uncertainties refer to these papers.

### *8.2. Results*

The resulting stellar parameters and chemical abundances of all program stars are given in Table 5. Effective temperatures turn out to range between $T_{\rm eff} = 20\,700 - 30\,800$ K, gravities between $\log g = 3.34 - 4.39$. Corresponding spectral types B0–1.5 V and B0.5–B1 III are derived from the scaling of Humphreys & McElroy (1984).

Stellar masses $M = 8 - 19\,{\rm M}_\odot$ and ages $\log\tau < 7.25$ are determined by comparison with standard single-star evolutionary tracks of $Z = 0.020$ (Schaller et al. 1992) and $Z = 0.008$ (Schaerer et al. 1993) (Fig. 9). Care has been taken to select a track of appropriate metallicity (via interpolation) for each star corresponding to its mean abundances derived. Note that *all* stars in Fig. 9 are precisely confined to the main-sequence phase predicted by stellar-evolution theory. Even the three low-$\log g$ stars formally ascribed to the luminosity class III are most probably ordinary main-sequence stars. Similarly, most of the high-$\log g$ stars are well described by tracks of sub-solar metallicity.

The microturbulences are $\xi = 1 - 13\,{\rm km\,s^{-1}}$, mostly less than $4\,{\rm km\,s^{-1}}$. This is about $10\,{\rm km\,s^{-1}}$ less than in typical LTE analyses (e.g. Kaufer et al. 1994). It is tempting to conclude that most, but not all of the apparent LTE microturbulence is absorbed by a proper non-LTE treatment of the problem. Rotational velocities $v\,\sin i = 20 - 80\,{\rm km\,s^{-1}}$ are within the expected range. However, this simply reflects the fact that we had actually selected slow rotators suitable for line analysis in preliminary low-resolution studies. In general, early B main-sequence stars have quite larger rotational velocities.

The line fits corresponding to those given for SH 2-208/6 in Fig. 10 generally are equally satisfactorily for all the other program stars, rather independently of their signal-to-noise ratio $S/N = 60 - 400$. In this way, we are quite confident in our method of analysis applied. However, the small deviation in the very core of H$\gamma$ visible in Fig. 10 for our example star equally applies for each star of the sample. This missing line core seems to occur independently of $T_{\rm eff}$ and $\log g$ to about the same extent.

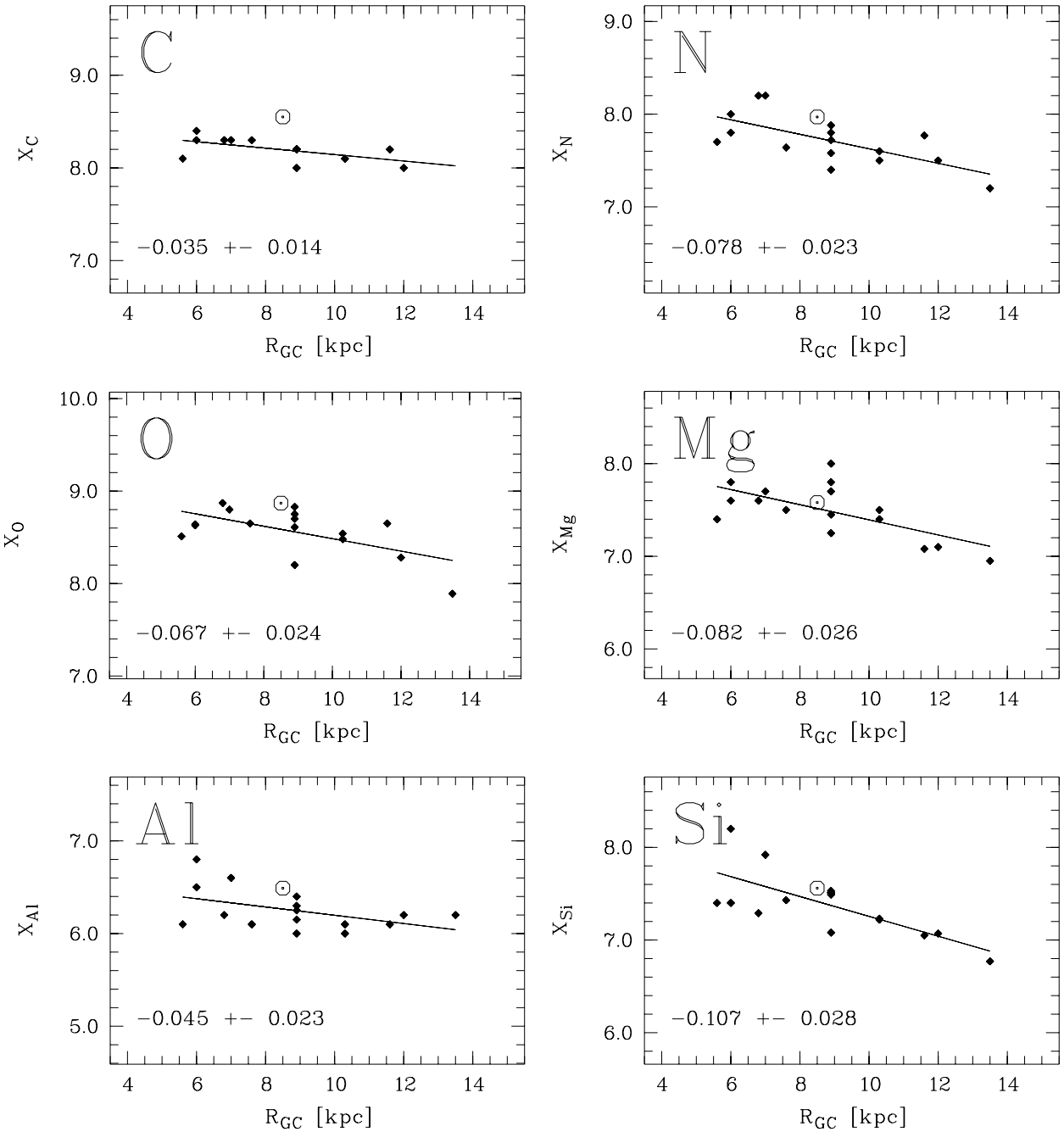


**Fig. 11.** Chemical-abundance gradients in the Galactic disk for the elements C, N, O, Mg, Al, and Si derived from the observational sample. $X_i \equiv 12 + \log(N_i/N_{\rm H})$. Solar abundances ($\odot$) at $R_{\rm GC} = 8.5\,{\rm kpc}$ are from Grevesse et al. (1996). The single gradients are given with the corresponding error derived from the data and their errors in Table 5. Significant non-zero gradients are recognized for all elements.

The same behavior is essentially found by the B-star study of Vrancken et al. (1997) which also used DETAIL/SURFACE line formation. However, we do not consider this a serious problem for the outcome of the analysis. The line-profile fits of different ions and also the parameter-sensitive Balmer-line *wings* look very consistent. In addition, the central Balmer core comprises only a negligible range within the line profile, constituting a similar effect as the rotational broadening on Balmer lines quoted in Sect. 7.1.

The chemical abundances deserve special interest. The derived metallicities as function of galactocentric radius are given in Fig. 11 containing the key finding of the present paper. *We detect significant C, N, O, Mg, Al, and Si abundance gradients of the order* $\Delta$*[O/H]*$/\Delta R_{\rm GC} = (-0.07 \pm 0.02)\ {\rm dex/kpc}$ *for B stars in galactocentric distances* $R_{\rm GC} = 5 - 14\ kpc$. Reanalysing the Kaufer et al. (1994) objects ($R_{\rm GC} > 8\,{\rm kpc}$) alone would basically yield the same gradients. The gradients of the various elements only differ by a small amount. There is neither

a significant [N/O] gradient nor any N overabundance relative to the other elements, which could have pointed to a convective or rotation-induced mixing of CNO-cycle products to the stellar surface. The observational error being about 0.1 dex (Table 5), the HR stars located in the Orion region at $R_{\rm GC} = 8.9\,{\rm kpc}$ seem to reflect a notable intrinsic abundance scatter. The local field of B stars has an underabundance of about 0.2 dex relative to the Sun. A possible explanation for the overabundance of the Sun might be the diffusion of stellar orbits in the Galactic disk (Wielen et al. 1996). According to that the Sun would be born several kpc further towards the Galactic center, where the metal abundance had been higher, and diffused outwards during the past gigayears.

## 9. Discussion

The relatively steep Galactic abundance gradient of $-0.07\ {\rm dex/kpc}$ derived in the present paper is in agreement with the study of Smartt & Rolleston (1997), and in contrast to both the LTE study of Kaufer et al. (1994) and the non-LTE study of Kilian-Montenbruck et al. (1994) which determined an almost flat gradient of the order 0 to $-0.02\ {\rm dex/kpc}$. We have to understand how this discrepancy can arise. The present study differs from that of Kilian-Montenbruck et al. mainly by the account for possible deviations from solar metallicities in the computation of the atmosphere, from that of Kaufer et al. by the non-LTE effect, in addition. In order to clarify the relevant importance of both effects it is crucial to trace them through the entire course of analysis, at least qualitatively.

*(a) Non-LTE effect.* The non-LTE effect for metal lines is the larger the smaller the gravity (Fig. 5, bottom). Conducting the silicon analysis according to Sect. 7.2 curves of equal microturbulence as function of $T_{\rm eff}$ and $\log g$ result from the Si III/IV ionization equilibrium (Fig. 8, dashed). Since the non-LTE effect acts in about the same way to both ionization stages there is no significant change in the line ratios and therefore in the Si curves in Fig. 8. Differently the oxygen lines: because the non-LTE effect acts in about the same way to weak and strong lines, the increased non-LTE line width at fixed $T_{\rm eff}$, $\log g$, and $X_{\rm O}$ (Fig. 7, solid) must be compensated by a smaller microturbulence. Comparing the non-LTE line width (Fig. 4, bottom left) with the $\xi$ one (Fig. 4, top right) it turns out that the effect corresponds to about several ${\rm km\,s^{-1}}$ in microturbulence. Since the Balmer lines show only a small non-LTE influence, the $\xi$ (O II) curves in Fig. 8 (dotted) get smaller values by the non-LTE effect. In this way, the points of intersection with the $\xi$ (Si III/IV) curves (Fig. 8, dashed) occur further to the right in the diagram. In turn, the final intersection with the Balmer curves arises right above, at smaller $T_{\rm eff}$ and $\log g$. According to Fig. 7, in this case the Si and O abundances should increase. However, since they decrease by the non-LTE effect at fixed $T_{\rm eff}$, $\log g$, and $\xi$ (Fig. 7, solid), both effects cancel each other. We arrive at the important finding: *The non-*LTE *effect lowers the stellar parameters* $T_{\rm eff}$, $\log g$, *and* $\xi$ *but leaves the chemical abundances roughly unaffected (Fig. 8).* This provides a plausible explanation of why Kilian-Montenbruck et al. (1994) obtained about the same B-star abundances with a non-LTE analysis as Kaufer et al. (1994) with a LTE analysis, both using solar-metallicity atmospheres only.

*(b) Atmospheric-metallicity effect.* According to Fig. 5 (top left) the Si III line gets stronger with decreasing metallicity if $T_{\rm eff}$ exceeds the temperature of maximum line strength. If $T_{\rm eff}$ falls below, the Si III line gets weaker. That means that the lines of constant equivalent width (Fig. 6) are shifted to the left if the metallicity decreases. Since both Si III and Si IV act in the same way, the Si curves in Fig. 8 (dashed) shift to the left, as well. Note that this is in contrast to the non-LTE effect described above. Essentially, both effects act perpendicularly to each other (Fig. 5). In the oxygen analysis the decreased line width at fixed $T_{\rm eff} < 30\,000$ K, $\log g$, and $X_{\rm O}$ (Fig. 7, solid) must be compensated by a larger microturbulence. Fig. 4 shows that a 1-dex metallicity effect corresponds to about several ${\rm km\,s^{-1}}$ in microturbulence. In turn, the intersection between the Si+O and the Balmer curves (Fig. 8) shifts to higher $T_{\rm eff}$. However, since with decreasing metallicity the Balmer curves shift to higher $T_{\rm eff}$ and lower $\log g$, gravity keeps about constant and, in turn, the metal abundances in Fig. 7 decrease. We arrive at the finding: *The metallicity effect of a sub–solar-abundance atmosphere raises the stellar parameters* $T_{\rm eff}$ *and* $\xi$*, leaves* $\log g$ *roughly unaffected, and lowers the chemical abundances (Fig. 8).* Basically, this is a well-known result. Referring to the ZAMS lines in Fig. 9 it is just the shift towards higher effective temperature stellar-structure theory predicts for decreasing metallicity (e.g. Schaller et al. 1992). However, we disagree with the statement by Maeder & Conti (1994) who ascribe this phenomenon to a relatively higher hydrogen content (if helium and heavier elements are decreased) by an *increase* of electron-scattering opacity. In our view, it is simply the *decrease* of bound-bound and bound-free opacity at $\log\tau \approx 1$ (being still about a factor 10 larger than electron-scattering opacity in a B-star atmosphere at this depth), which just makes the metal-poor star smaller in radius. The metallicity effect provides a natural explanation for the steep abundance gradient of the present paper compared to Kilian-Montenbruck et al. (1994) and Kaufer et al. (1994). In the inner part of the Galaxy with its solar abundances all three methods—LTE + solar atmospheres, non-LTE + solar atmospheres, and non-LTE + variable atmospheres—yield the same abundances. However, the underabundance of the outer Galaxy is only detectable with non–solar-abundance atmospheres. *It is the consistency between atmosphere and line abundance in our study, which leads to a steep abundance gradient in the Galactic disk.* A proper comparison to the results of Smartt & Rolleston (1997) is hard to manage. Whereas we determine $T_{\rm eff}$, $\log g$, $\xi$, $X_{\rm O}$, and $X_{\rm Si}$ in a consistent manner described in Sect. 7.4, Smartt & Rolleston use the values of $T_{\rm eff}$ and $\log g$ derived in earlier LTE studies of their group to extract non-LTE oxygen abundances from the Becker & Butler (1988b) tabulation, assuming a constant microturbulence of $\xi = 5\ {\rm km\,s^{-1}}$ and solar atmospheres for all stars. Quite surprisingly, they obtain the same oxygen gradient of $-0.07\ {\rm dex/kpc}$ with their method as the present paper. According to the effects discussed above their LTE parameters

$T_{\rm eff}$ and $\log g$ could be overestimated yielding decreased abundances. This effect should be proportional to the non-LTE effect which increases with decreasing $\log g$. Indeed the three outermost stars in their sample show quite low gravities. In this way, it might be that a selection effect versus luminous stars with low $\log g$ is able to create an apparent abundance gradient, as well.

*(c) Galactic abundance determinations.* The derived steep abundance gradient $-0.07\,\mathrm{dex/kpc}$ well agrees with the classical results of Galactic H II regions by Shaver et al. (1983). A similar result is provided by Afflerbach et al. (1996, 1997) between 0 and 11 kpc galactocentric distance. The flat H II gradient between 6 and 10 kpc found by Simpson et al. (1995) has been revised by Rudolph et al. (1997) adding clear evidence for lower abundances between 10 and 16 kpc. Still Vílchez & Esteban (1996) derive a nearly constant O and N abundance in H II regions between 11 and 18 kpc. Therefore, almost all recent young-population studies—B stars and H II regions—derive steep gradients, at least for $R_{\rm GC} < 10\,\mathrm{kpc}$. The same do old-population studies quoting planetary nebulae (Maciel & Köppen 1994), old open clusters (Friel 1995; Twarog et al. 1997), and F and G dwarfs in the solar neighborhood (Edvardsson et al. 1993). They generally find gradients of the order $-0.06$ to $-0.10\,\mathrm{dex/kpc}$. It is tempting to conclude that the abundance gradient of the Galactic disk did not significantly change during the past gigayears. Additionally, from the work of Edvardsson et al. (1993) covering an age range of 2-15 Gyr (e.g. Fig. 5 in Prantzos & Aubert 1995) one might infer an increase of absolute metal abundance of about $+0.04\,\mathrm{dex\,Gyr^{-1}}$. Contrary, Mollá et al. (1997) and Allen et al. (1998) find evidence that the abundance gradient tends to flatten, Chiappini et al. (1997) to steepen with time.

*(d) Chemical-evolution calculations.* Such computations are hampered by the number of input parameters entering the evolution codes. Often they are coupled to specific observational data. Far from being complete, we only mention that from the comprehensive review of Tosi (1996) there might be a reasonable agreement between the observational evidence quoted above and the evolutionary models of Matteucci & François (1989) which predict a time-independent gradient of the relevant order of magnitude. For future research, multi-dimensional approaches to the chemical evolution of the Galaxy (e.g. Samland et al. 1997) will be valuable tools.

*(e) External galaxies and the bar structure of the Galaxy.* In Sect. 2.4 we asked if the Galactic abundance gradient is $-0.02$ or $-0.07\,\mathrm{dex/kpc}$. Apparently, the observational evidence points to the latter. According to Vila-Costas & Edmunds (1992) and Zaritsky et al. (1994) a gradient of $-0.07\,\mathrm{dex/kpc}$ is typical for a normal spiral galaxy of Hubble type Sbc. For a barred spiral galaxy of type SBbc, however, such a steep gradient seems to be amazing. Then, how does the Milky Way manage to possess such a strong spatial variation in abundances in spite of the evidence for its central bar structure (Kuijken 1996; Gerhard et al. 1998)? A possible solution might be found in the numerical simulations of the chemodynamical evolution of barred galaxies by Martinet & Friedli (1997). They show that a typical bar structure with a disk gradient of $-0.07\,\mathrm{dex/kpc}$ and a bar axis ratio of $b/a = 1/2$ is only about 1 Gyr old. This could mean that the bar of the Milky Way did not have enough time until now to produce a chemical homogenization of the Galactic disk as seen in theoretical models (Friedli et al. 1994; Friedli & Benz 1995) and observations of barred galaxies (Vila-Costas & Edmunds 1992; Martin & Roy 1994, 1995). In this way, it is only natural to assume that our gradient might soonly flatten during the next several hundred Myr. As driving agent for the formation of the Galactic bar it is tempting to invoke close encounters of the Galactic disk with the Magellanic clouds as described in the simulations by Gardiner et al. (1994) and Gardiner & Noguchi (1996). Further evidence for such a scenario is provided by Elson et al. (1997) who determine the age of the bar structure of the Large Magellanic Cloud to about 1 Gyr, which is in accordance with the age of the Galactic bar structure derived above.

*Acknowledgements.* We like to thank B. Baschek, D. Husfeld, S. Becker, K. Butler, and A. Jüttner for their encouraging support. The present study has been supported by the Deutsche Forschungsgemeinschaft DFG (Wo 296/18-1) and the Sonderforschungsbereich SFB 328 "Entwicklung von Galaxien".

## References

Afflerbach A., Churchwell E., Acord J.M., Hofner P., Kurtz S., De Pree C.G., 1996, ApJS 106, 423
Afflerbach A., Churchwell E., Werner M.W., 1997, ApJ 478, 190
Allen C., Carigi L., Peimbert M., 1998, ApJ 494, 247
Anderson, 1985, ApJ 298, 848
Bailer-Jones C.A.L., Irwin M., Gilmore G., von Hippel T., 1997, MNRAS 292, 157
Baschek B., Holweger H., Traving G., 1966, Abhandl. Hamburger Sternwarte VIII, Nr. 1, 26
Becker S.R., 1997, priv. comm.
Becker S.R.; Butler K., 1988a, A&A 201, 232
—, 1988b, A&AS 74, 211
—, 1988c, A&AS 76, 331
—, 1989, A&A 209, 244
—, 1990a, A&AS 84, 95
—, 1990b, A&A 235, 326
Belley J., Roy J.-R., 1992, ApJS 78, 61
Butler K., 1984, PhD Thesis, University of London
—, 1994. ftp://ccp7.arm.ac.uk/ccp7/Docs/detail.ps
—, 1996, priv. comm.
Butler K., Giddings J.R., 1985, CCP7 Newsletter 9, 7
Carraro G., Chiosi C., 1994, A&A 287, 761
Castelli F., Kurucz R.L., 1994, A&A 281, 817
Chiappini C., Matteucci F., Gratton R., 1997, ApJ 477, 765
Dreizler S., Werner K., 1993, A&A 278, 199
Eber F., Butler K., 1988, A&A 202, 153
Edvardsson B., Andersen J., Gustafsson B., Lambert D.L., Nissen P.E., Tomkin J., 1993, A&A 275, 101
Elson R.A.W., Gilmore G.F., Santiago B.X., 1997, MNRAS 289, 157
Fich M., Silkey M., 1991, ApJ 366, 107
Friedli D., Benz W., 1995, A&A 301, 649
Friedli D., Benz W., Kennicutt R., 1994, ApJ 430, L105
Friel E.D., 1995, ARA&A 33, 381
Fux R., 1997, A&A 327, 983
Gardiner L.T., Noguchi M., 1996, MNRAS 278, 191
Gardiner L.T., Sawa T., Fujimoto M., 1994, MNRAS 266, 567

Gehren T., 1988, Rev. Mod. Astron. 1, 52
Gerhard O.E., 1996. In Blitz L., Teuben P. (eds.) Unsolved Problems of the Milky Way, Kluwer, Dordrecht, p. 79
Gerhard O.E., Binney J., Zhao H., 1998. In Andersen J. (ed.) Highlights of Astronomy 11, Kluwer, Dordrecht, in press
Giddings J.R., 1981, PhD Thesis, University of London
Gold M., 1984, Diploma Thesis, Universität München
Grevesse N., Noels A., Sauval A.J., 1996. In Holt S.S., Sonneborn G. (eds.) Cosmic Abundances, Astronomical Society of the Pacific, San Francisco, p. 117
Grigsby J.A., Morrison N.D., Anderson L.S., 1992, ApJS 78, 205
Gummersbach C.A., Zickgraf F.-J., Wolf B., 1995, A&A 302, 409
Gummersbach C.A., Kaufer A., 1996. http://www.lsw.uni-heidelberg.de/cgi-bin/cgiwrap/ostahl/websynspec.cgi
Henry R.B.C., Howard J.W., 1995, ApJ 438, 170
Hubeny I., Lanz T., 1992, A&A 262, 501
Humphreys R.M., McElroy D.B., 1984, ApJ 284, 565
Husfeld D., 1996, priv. comm.
Jeffery C.S., 1993. ftp://ccp7.arm.ac.uk/ccp7/Soft/detail.read.me
—, 1996, QJRAS 37, 39
Kaufer A., 1998, Rev. Mod. Astron. 11, in press
Kaufer A., Szeifert T., Krenzin R., Baschek B., Wolf B., 1994, A&A 289, 740
Kilian-Montenbruck J., Gehren T., Nissen P.E., 1994, A&A 291, 757
Kudritzki R.P., Hummer D.G., 1990, ARA&A 28, 303
Kuijken K., 1996. In Buta R., Crocker D.A., Elmegreen B.G. (eds.) Barred Galaxies, Astronomical Society of the Pacific, San Francisco, p. 504
Kurucz R.L., 1979, ApJS 40,1
—, 1991a. In Crivellari L., Hubeny, I., Hummer D.G. (eds.) Stellar Atmospheres - Beyond Classical Models, Kluwer, Dordrecht, p. 441
—, 1991b. In Philip A.G.D., Upgren A.R., Janes K. (eds.) Precision Photometry - Astrophysics of the Galaxy, L. Davis, Schenectady, p. 27
—, 1992. In Barbuy B., Renzini A. (eds.) The Stellar Populations of Galaxies, Kluwer, Dordrecht, p. 225
—, 1993a. Kurucz CD-ROM No. 13 - ATLAS 9 Stellar Atmosphere Programs and 2 km/s Grid, Smithonian Astrophysical Observatory, Cambridge
—, 1993b. Kurucz CD-ROM No. 2 - Opacities for Stellar Atmospheres: [+0.0],[+0.5],[+1.0], Smithonian Astrophysical Observatory, Cambridge
—, 1993c. Kurucz CD-ROM No. 3 - Opacities for Stellar Atmospheres: [-0.5],[-1.0],[-1.5], Smithonian Astrophysical Observatory, Cambridge
Kurucz R.L., Bell B., 1995, Kurucz CD-ROM No. 23 - Atomic Line List, Smithonian Astrophysical Observatory, Cambridge
Kurucz R.L., Peytremann E., 1975, SAO Spec. Rep. 362, 1219
Lahulla J.F., 1985, A&AS 61, 537
Lemke M., 1995. ftp://ccp7.arm.ac.uk/ccp7/Soft/atlas.unix.tar.Z
Maciel W.J., Köppen J., 1994, A&A 282, 436
Maeder A., Conti P.S., 1994, ARA&A 32, 227
Martin P., Roy J.-R., 1994, ApJ 424, 599
—, 1995, ApJ 445, 161
Martinet L., 1995, Fund. Cosmic Phys. 15, 341
Martinet L., Friedli D., 1997, A&A 323, 363
Matteucci F., 1996, Fund. Cosmic Phys. 17, 283
Matteucci F., François P., 1989, MNRAS 239, 885
McWilliam A., 1997, ARA&A 35, 503
Moffat A.F.J., Vogt N., 1973, A&AS 10, 135
Moffat A.F.J., Vogt N., 1975, A&AS 20, 85
Mollá M., Ferrini F., Díaz A.I., 1997, ApJ 475, 519
Monteverde M.I., Herrero A., Lennon D.J., Kudritzki R.-P., 1997, ApJ 474, L107
Noguchi M., 1996, ApJ 469, 605
Oey M.S., Kennicutt R.C., 1993, ApJ 411, 137
Pagel B.E.J., 1997, Nucleosynthesis and Chemical Evolution of Galaxies, Cambridge University Press, Cambridge
Pasquini L., 1993, CASPEC – Update to the Operating Manual, European Southern Observatory, Garching
Peytremann E., Baschek B., Holweger H., Traving G., 1967, Un Program FORTRAN d'Analyse Quantitative des Spectres Stellaires, Obs. Genève.
Prantzos N., Aubert O., 1995, A&A 302, 69
Raboud D., Grenon M., Martinet L., Fux R., Udry S., 1998, A&A 335, L61
Rivinius T., Baade D., Stefl S., Stahl O., Wolf B., Kaufer A., 1998, A&A 333, 125
Roy J.-R., Walsh J.R., 1997, MNRAS 288, 715
Roy J.-R., Belley J., Dutil Y., Martin P., 1996, ApJ 460, 284
Rudolph A.L., Simpson J.P., Haas M.R., Erickson E.F., Fich M., 1997, ApJ 489, 94
Samland M., Hensler G., Theis C., 1997, ApJ 476, 544
Schaerer D., Meynet G., Maeder A., Schaller G., 1993, A&AS 98, 523
Schaller G., Schaerer D., Meynet G., Maeder A., 1992, A&AS 96, 269
Sellwood J.A., Wilkinson A., 1993, Rep. Prog. Phys. 56, 173
Shaver P.A., McGee R.X., Newton L.M., Danks A.C., Pottasch S.R., 1983, MNRAS 204, 53
Simpson J.P., Colgan S.W.J., Rubin R.H., Erickson E.F., Haas M.R., 1995, ApJ 444, 721
Skillman E.D., Kennicutt R.C., Shields G.A., Zaritsky D., 1996, ApJ 462, 147
Smartt S.J., Rolleston W.R.J., 1997, ApJ 481, L47
Tosi M., 1996. In Leitherer C., Fritze-von Alvensleben U., Huchra J. (eds.) From Stars to Galaxies. Astronomical Society of the Pacific, San Francisco, p. 299
Twarog B.A., Ashman K.M., Anthony-Twarog B.J., 1997, AJ 114, 2556
Vila-Costas M.B., Edmunds M.G., 1992, MNRAS 259, 121
Vílchez J.M., Esteban C., 1996, MNRAS 280, 720
Vrancken M., Hensberge H., David M., Verschueren W., 1997, A&A 320, 878
Wielen R., Fuchs B., Dettbarn C., 1996, A&A 314, 438
Zaritsky D., Kennicutt R.C., Huchra J.P., 1994, ApJ 420, 87